Multiple-axle box acceleration measurements at railway transition zones

Unsiwilai, S.; Wang, L.; Nunez, Alfredo; Li, Z.

DOI
10.1016/j.measurement.2023.112688

Publication date
2023

Document Version
Final published version

Published in
Measurement

Measurement 213 (2023) 112688

Contents lists available at ScienceDirect

Measurement

journal homepage: www.elsevier.com/locate/measurement

Multiple-axle box acceleration measurements at railway transition zones

Siwarak Unsiwilai [a], Li Wang [a], Alfredo Núñez [a], Zili Li [a,*]

[a] Section of Railway Engineering, Department of Engineering Structures, Faculty of Civil Engineering and Geosciences, Delft University of Technology, Stevinweg 1, 2628 CN Delft, the Netherlands

ARTICLE INFO

Keywords:
Transition zones
Railway infrastructure
Axle box acceleration
Time-frequency analysis
Onboard measurement

ABSTRACT

This paper presents a methodology for monitoring transition zones using responses of multiple-axle box acceleration (multi-ABA) measurements. The time–frequency characteristics of the vertical ABA signals from four wheelsets are analyzed. The major contributions are as follows. (1) We propose four key performance indicators (KPIs) to quantify local multi-ABA energy differences at different abutments, tracks, entrance and exit sides, and inner and outer rails. (2) The same dominant spatial frequencies are obtained with different measurement speeds, so the proposed method is suitable for multi-ABA systems mounted on operational trains. Transition zones at nine double-track railway bridges are selected as the case study. The KPIs indicate that (1) the energy differences between abutments are above 80% in three bridges; (2) two abutments show that the energy differences between tracks are higher than 100%; (3) three tracks have energy differences above 100% between the entrance and exit sides; and (4) the energy differences between rails are above 80% on three sides. Finally, using measurement with 7 years of difference, the KPIs and track quality index are discussed. These findings suggest that multi-ABA measurement can be used as a health condition monitoring method for railway transition zones to support condition-based maintenance.

1. Introduction

Railway transition zones are the segments between the conventional track and rigid structures, such as bridges, tunnels, and culverts. The degradation of track geometries at transition zones usually occurs much faster than at other locations [1–8]. For example, in the Netherlands, it has been reported that the maintenance frequency at transition zones can be 2–8 times that for typical tracks [9]. This frequent maintenance is very costly and largely reduces track availability.

The fast degradation of transition zones has attracted extensive worldwide attention from the railway community. The literature on railway transition zones covers various approaches for understanding the corresponding behavior, such as modeling [10–17] and monitoring [18–24]. The fast degradation at railway transition zones is mainly attributed to the variation in track support [2,19,25–29].

In addition to differential track support, degradation can occur from secondary causes, such as a poor ballast layer, an insufficient lateral rail constraint, an embankment foundation that is too soft, train speeds higher than the design speed, and an excessively heavy train axle load [2,25]. Therefore, a particular transition zone needs customized solutions because of its specific designs, structures, bearing capacity, soil conditions, etc. Each country has regulations for designing and constructing railway transition zones [25]. The maintenance solutions for transition zones have varied from ballast tamping or stone blowing [30] to the use of under sleeper pads [31], ballast glue with polymers [32], auxiliary rails [33], and adjustable fasteners [34].

These different solutions combined with the functional service conditions of the transition zones make the corresponding health monitoring task complex. Researchers in the railway field aim extract valuable and practical information from transition zones from various measurements. At present, many measurement techniques have been developed to monitor the health conditions of railway transition zones, including trackside and onboard measurement techniques [35]. Trackside measurements can monitor responses from instrumented transition zones at specific locations and subsequently interpret them into health condition indicators. Every train passage generates the excitation required to acquire health condition information. In the case of onboard measurements, every train passage acquires information from all the transition zones it visits. In particular, sensors mounted on the vehicle capture the responses related to the train-track interaction. These measurements contain the whole track system response. Identifying which parts of the responses are related to each track component can be

* Corresponding author.
E-mail addresses: S.Unsiwilai@tudelft.nl (S. Unsiwilai), L.Wang-7@tudelft.nl (L. Wang), A.A.NunezVicencio@tudelft.nl (A. Núñez), Z.Li@tudelft.nl (Z. Li).

https://doi.org/10.1016/j.measurement.2023.112688
Received 19 July 2022; Received in revised form 18 February 2023; Accepted 5 March 2023
Available online 17 March 2023

challenging, especially in terms of low and middle frequency ranges [36–39]. Track monitoring benefits from both trackside and onboard measurements. In this paper, we focus on onboard sensing, considering that nowadays, most rolling stock manufacturers are already instrumenting all their rolling stocks, while campaigns for the instrumentation of each and every transition zone still have open challenges when thinking of massive instrumentations in large-scale networks. In [18], a 1-year monitoring campaign of a transition zone at a culvert with concrete approach slabs was conducted considering the vertical displacement and settlement using geophones, accelerometers, and pore water pressure sensors. The results showed that poor performance in the vertical displacement was due to the settlement and rotation of one approach slab. In [19], six months of field monitoring indicated that hanging sleepers or sleepers in poor support conditions were a direct cause of permanent vertical deformation in transition zones. Poor sleeper support increases the applied stress from the sleeper to the ballast. In [20], a monitoring framework was developed to assess the performance of transition zones at culverts. The framework included measurements based on the track dynamic flexibility using hammer tests, vertical acceleration, and displacement responses of the track components (rails, sleepers) using linear variable differential transformers (LVDTs) and a laser-based position-sensitive detector. In [40], a measurement campaign was described for assessing the performance of the novel solution of the transition zone. The responses of track components, including vertical acceleration of sleepers, vertical displacement of sleepers, rails shear stress, and vertical displacement of rails, were selected for the assessment. In [41], three transition zones with different structural details were instrumented with accelerometers at sleepers at the bridge, transition zone, and open track to assess their performance. The results showed that sleeper acceleration of the well-performed transition zone was less than 5 g, which was similar to the responses of a sleeper on the open track. In contrast, transition zones with track geometry problems were found to provide sleeper acceleration higher than 10 g. In [42], so-called multidepth deflectometers (MDDs) were introduced to the research framework to investigate differential movement in railway transitions. Then, in [43], MDDs were used to monitor track substructure settlement at different layers. The measurement consisted of permanent deformation monitoring and transient deformation corresponding to the train load. The findings showed that the ballast layer was the most deformed for both accumulated permanent and transient deformations. In addition, digital image correlation (DIC) [44,45], satellite synthetic aperture radar (InSAR) [46], smartphones [47], and geometry measurements [48] have been used to monitor the differential settlement, settlement rate, and other characteristics in transition zones. The methods discussed above have general drawbacks, such as complex measurement procedures with high costs, low data acquisition and transmission efficiency; or a limitation to the geometry state instead of structural conditions. The latest sensing techniques and Internet of Things (IoT) developments are expected to enable full instrumentation of railway bridge transition zones and automatic processing of frequent measurements [49–51].

The present study considers a multiple-axle box acceleration (multi-ABA) monitoring technique that relies on onboard measurements and has been implemented on operational trains, enabling frequent condition monitoring of transition zones and other railway track components. The axle box acceleration (ABA) measurement method was developed for railway track defect detection [52–54]. With this method, the local dynamic response deviation can be evaluated and compared to the measurements obtained under healthy conditions. In previous studies, ABA measurements were used to detect squats in rail surfaces, perform condition assessments of insulated rail joints, welds, crossing noses, and measure joint bolt tightness [55–59]. The high-frequency range of ABA is fundamental for detecting the abovementioned shortwave irregularities. The present study is intended to characterize the ABA responses at railway bridge transition zones as case studies to allow further developments of condition-based assessments of railway transition zones and maintenance solutions, especially substructures that consist of layers of ballast, subballast, and subgrade [60]. Note that in some reports, the subballast and ballast were considered part of the superstructure.

The present paper focuses on the spatial frequency range from 0.04 m^{-1} to 0.33 m^{-1}, corresponding to the D1 wavelength range of track longitudinal irregularities from 3 m to 25 m [61]. This longitudinal wavelength range has been reported to be dominated by substructure variations [62,63], is used as one of the criteria for measuring tamping activity [64], and is used for the analysis of track settlement modeling [65]. Multi-ABA measurements include acceleration signals in the vertical direction on multiple wheelsets; such signals are considered the primary input to define the responses of railway transition zones. Then, multi-ABA signal responses at different transition zone locations are analyzed. It has been reported that more severe track conditions cause higher dynamic wheel loads [64]. Thus, a method is proposed here to compare the degradation level of transition zones at a particular bridge based on ABA energy, as larger ABA energies should be observed for tracks with more degradation. We propose four key performance indicators (KPIs) based on multi-ABA measurements to evaluate the differences in energy levels between different abutments, tracks, sides, and rails at each bridge.

This paper is organized as follows. The proposed methodology for monitoring railway transition zones using multi-ABA is presented in Section 2. Section 3 describes an analysis of multi-ABA signals from different wheelsets and different measurement speeds. Next, the responses of multi-ABA signals at various transition zone study areas are analyzed in Section 4. Section 5 presents results from the degradation level evaluation of transition zones using KPIs based on multi-ABA measurements. Finally, the conclusion of this study and suggestions for further research are presented in Section 6.

2. Multi-ABA measurement method at transition zones

The methodology of this study is shown in Fig. 1. The first step is data collection. Next, wavelets are used to extract multi-ABA signal characteristics, and the multi-ABA responses are analyzed at various locations of a particular railway bridge. Finally, the condition of railway transition zones is evaluated using the ABA energy as the basis of four KPIs that quantify differences between abutments, tracks, sides, and rails.

2.1. Data collection at railway transition zones

The ABA measurement system [66] consists of three major components. First, 1-directional accelerometers with linear characteristics up to 10 kHz are attached and aligned with the center of each axle box in the vertical and longitudinal directions, with respect to the train travel direction. Second, a global positioning system (GPS) antenna and tachometer are used to determine the position and running speed of the measurement train. Third, an NI compact RIO data acquisition system records signals with synchronized sampling between all channels. The acceleration at time instant t for wheelset w and rail r is defined as $a_{w,r}(t)$. Eight acceleration signals from four wheelsets $w \in \{w1, w2, w3, w4\}$ and the inner (I) and outer (O) rails $r \in \{I, O\}$ are considered. The front wheelset at the front bogie is $w1$, the rear wheelset at the front bogie is $w2$, the front wheelset at the rear bogie is $w3$, and the rear wheelset at the rear bogie is $w4$. The location of the wheelset w at time instant t is $x_w(t)$. Then, after synchronizing the signals, the acceleration signals can be evaluated as a function of the track location x, $a_{w,r}(x)$. According to the system configuration, the measurement system records ABA signals with a sampling rate of 25.6 kHz. However, several studies have reported that the track substructure vibration responses occur in a frequency range below 100 Hz [67–69]. In this study, the considered wavelength λ of track irregularities is from 3 m to 25 m. These irregularities are the excitation, and the corresponding passing frequency f at speed V of the measurement train is:

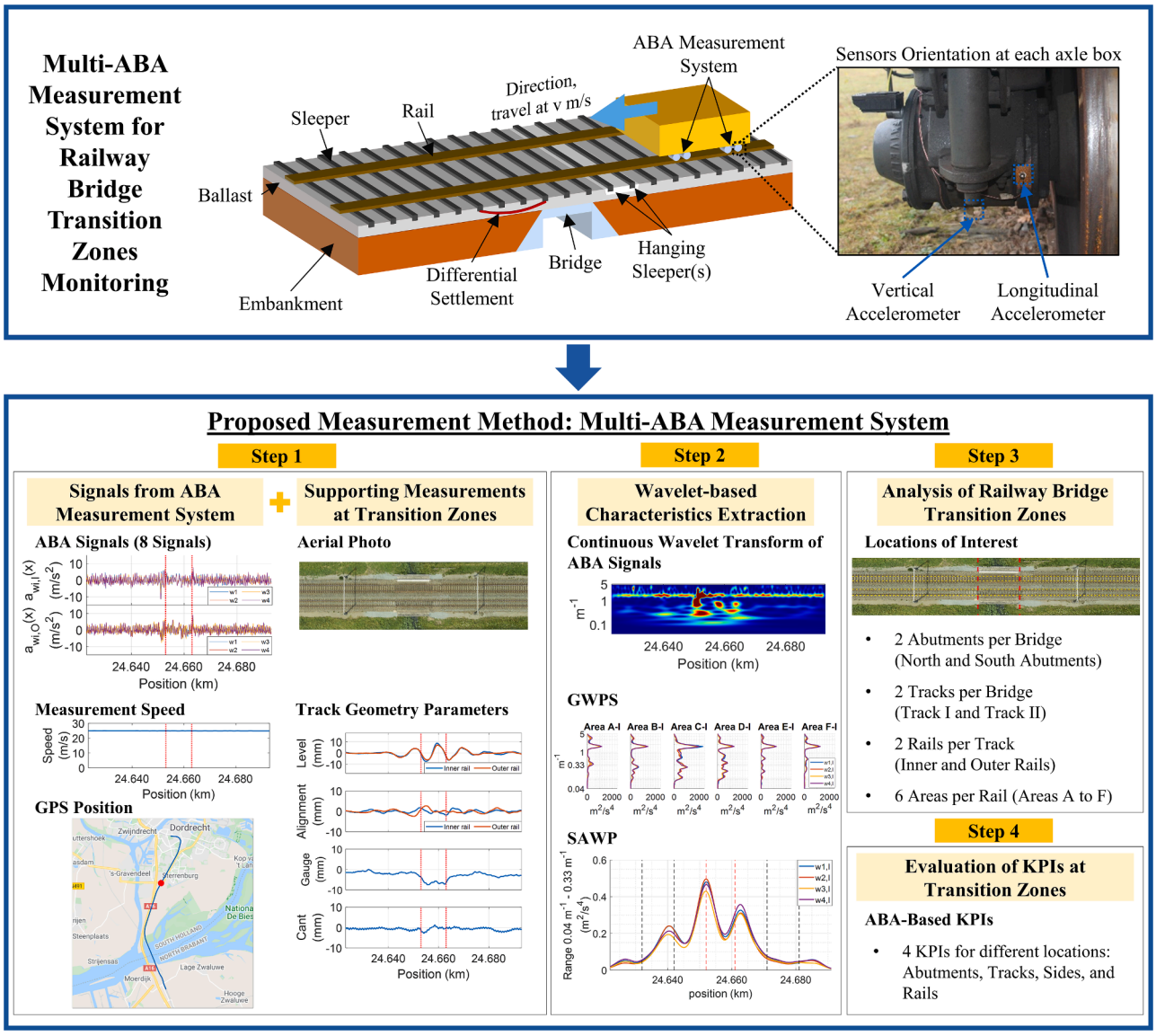

Fig. 1. Proposed methodology of this study. ABA signals with 100 Hz cutoff frequency are used in the figures of this paper (source of aerial photographs: BBMS, ProRail, source of background map: Google Maps).

$$f = \frac{V}{\lambda} \tag{1}$$

The maximum operating speed in the conventional Dutch railway network is 140 km/h. Therefore, the corresponding frequencies of interest are on the order of 12.96 Hz. A 4th-order Butterworth low-pass filter with 100 Hz cut-off frequency is used to preprocess the measured ABA signals to cover the considered dynamic responses.

In addition, supporting information is considered from the Dutch railway infrastructure monitoring database, called the Branche Breed Monitoring Systeem (BBMS, in Dutch), including aerial photographs and track geometry measurements. The track geometry measurements include six parameters: The longitudinal level of inner rail and outer rail (deviation of the top of rail head in the vertical direction from the reference line), alignment of inner rail and outer rail (deviation of the side of rail head in the lateral direction from the reference line), track gauge (perpendicular distance between the inner side of rail head), and cant (different height between the top of rail heads). The data are all positioned in the Dutch railway reference system.

2.2. Response extractions using the wavelet

ABA signals are nonstationary and capture the track characteristic frequency responses at different locations. One of the well-known methods for analyzing these local variations is wavelet analysis. The continuous wavelet transform (CWT) converts the acceleration signals into energy at a specific location and frequency based on a group of shifted and scaled wavelet functions. The CWT is defined in [70] as follows:

$$CWT_{w,r}(x,s) = \sum_{n'=0}^{N-1} a_{w,r}(n')\psi^*\left(\frac{(n'-n)\delta_t}{s}\right) \tag{2}$$

where $CWT_{w,r}(x,s)$ is the wavelet coefficient of the acceleration signal from wheel w and rail r at location x and wavelet scale s with $s > 0$, N is the number of data points in a considered time frame, $n' = 0,\ldots,N-1$, $a_{w,r}(n')$ is the ABA signal at instant $t = n'$, n is the time index variable for the continuous translation, δ_t is the time interval between data points, and ψ is the wavelet mother function. The function ψ^* is a family of wavelets derived from the mother wavelet by translations and scaling,

and $*$ refers to the complex conjugate. In this paper, the Morlet function is used as the mother wavelet. Finally, the wavelet power spectrum (WPS) is defined as the square of the absolute wavelet coefficients:

$$WPS_{w,r}(x,s) = \left|CWT_{w,r}(x,s)\right|^2 \tag{3}$$

where $WPS_{w,r}(x,s)$ is the WPS of the acceleration signal from wheel w and rail r at location x and wavelet scale s with $s > 0$. The scalogram, a plot representing a function of time and frequency, is used to visualize the WPS. Instead of the time domain, the space domain, according to the track position, is used at each instance. Moreover, the spatial frequency (m^{-1}), the inverse of the wavelength obtained by dividing the measured frequency by the measured speed, is considered due to the speed differences between different measurements. Therefore, the scalogram in the space domain function and the spatial frequency domain are used instead of the time and frequency domains. This modified scalogram can reflect the primary track responses with various measurement speeds at different locations.

Then, the global wavelet power spectrum (GWPS) is used to evaluate an average of the WPS within a particular segment of positions, calculated as follows:

$$GWPS_{w,r}(s) = \frac{1}{n_2 - n_1}\sum_{n=n_1}^{n_2} WPS_{w,r}(x_n, s), \quad x_{n_1} < x_n < x_{n_2} \tag{4}$$

where $GWPS_{w,r}(s)$ is the GWPS of the acceleration signal from wheel w and rail r, within the location from x_{n_1} to x_{n_2}, for wavelet scale s with $s > 0$, $WPS_{w,r}(x_n, s)$ is the wavelet power spectrum at position x_n, and n_1 and n_2 are selected according to the preferred window length of the analysis.

Finally, the scale average wavelet power (SAWP) is used to investigate the WPS within a considered spatial frequency range and can be defined as follows:

$$SAWP_{w,r}(x) = \frac{\delta_j \delta_t}{C_\delta}\sum_{j=j_1}^{j_2} \frac{WPS_{w,r}(x, s_j)}{s_j} \tag{5}$$

where $SAWP_{w,r}(x)$ is the SAWP of the acceleration signal from wheel w and rail r, at location x and within the wavelet scale s from s_{j_1} to s_{j_2}, $WPS_{w,r}(x, s_j)$ is the wavelet power spectrum at scale j, δ_j is the scale step, δ_t is the time step, and C_δ is the empirically derived constant of the wavelet function.

2.3. Railway bridge transition zones

This study aims to provide solutions for monitoring substructure at conventional railway lines, particularly due to the generally poor bearing capacity of the Dutch soil. In this paper, we first consider the challenges at bridge transition zones. At those locations, a sharp change in track stiffness occurs, and the lower frequency responses of ABA show a dramatic change, where ballast, subballast, and subgrade responses dominate. This studied railway line is double-track with fixed travel directions; see Fig. 2. Track I is for trains traveling from Lage Zwaluwe to Dordrecht, and Track II is for trains traveling from Dordrecht to Lage Zwaluwe. The health condition of the transition zones is estimated by analyzing the measurements at different locations. These locations include the entrance and exit sides on each of the two tracks, abutments (dashed red lines in Fig. 2), and the inner and outer rails (dashed yellow lines in Fig. 2). A segment length of 30 m was reported to be sufficient for investigating transition zones [2,17,71], in line with the maximum wavelength of 25 m of interest. Thus, track sections are analyzed at both ends of the bridge, from 30 m before the abutment on the entrance side to 30 m from the abutment on the exit side. Analysis of the energy content of the multi-ABA signals indicated that 53% of the energy is concentrated in the first 10 m next to the bridge. Thus, we analyze six areas that are 10 m in length at the entrance side (Areas A-I to C-I for Track I and Areas A-II to C-II for Track II) and the exit side (Areas D-I to F-I for Track I and Areas D-II to F-II for Track II). The partitioning of 10 m helps visualize the spatial characteristics of transition zones. The farther the zone is from the bridge (zones A and F), the closer the response is to the conventional track. Further, the estimation of SAWP and wavelet responses from multi-ABA measurements do not require the proposed partitioning for analysis.

2.4. Case studies of railway bridge transition zones

Transition zones at nine railway bridges between Dordrecht station and Lage Zwaluwe station, denoted as Bridge 1 to Bridge 9, are selected

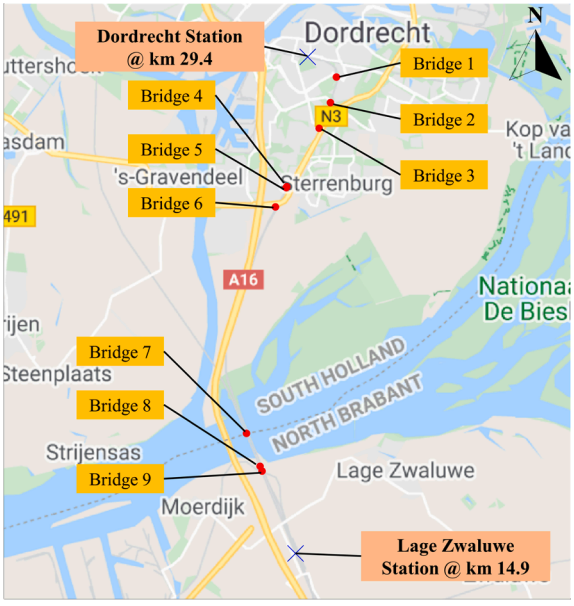

Fig. 3. Location of bridges between Dordrecht station and Lage Zwaluwe station (source of the background map: Google Maps).

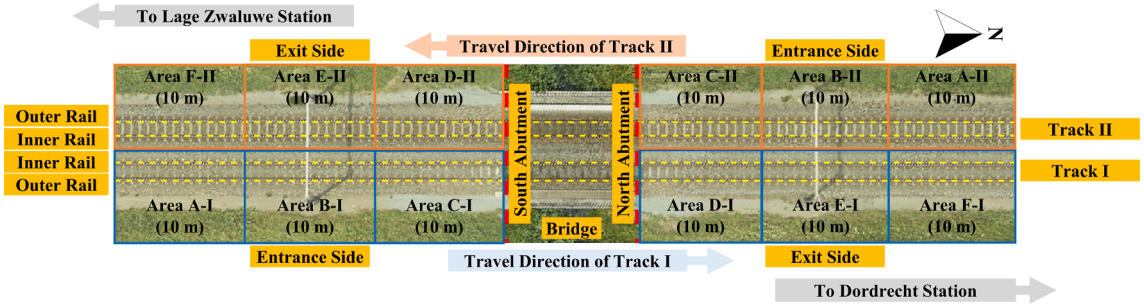

Fig. 2. Study areas of transition zones at the double-track railway bridge (source of aerial photographs: BBMS, ProRail).

as the case studies. Fig. 3 presents a map of the bridge locations, which are indicated with red dots. Bridges 1, 2, and 3 are bridges that cross urban roads in the city of Dordrecht. Bridges 4 and 6 cross over small waterways. Bridge 5 crosses over bicycle paths. Bridge 7 is the Moerdijk bridge that crosses the river Hollands Diep. Bridge 8 crosses a rural road, and Bridge 9 crosses a regional railway track.

Table 1 shows detailed information for each bridge, including aerial photographs and side view photographs. The measurement campaign was conducted at both tracks in April 2019. Two measurements are available for Track I (between Lage Zwaluwe and Dordrecht), denoted as Track I#1 and Track I#2. The two additional measurements for Track II (between Dordrecht and Lage Zwaluwe) are called Track II#1 and Track II#2. Fig. 4 shows the speed profile of the measurements and the averaged speed over 30 m when the train enters and exits the bridges.

3. Multi-ABA responses from different wheelsets and measurement speeds

This section analyzes the ABA signals from different wheelsets and different measurement speeds. To showcase the analysis of different wheelsets, signals from the inner rail at the transition zones of Track I at Bridge 6, measured at a speed of 24.9 m/s (Track I#1), are selected. Bridge 6 is selected because it is relatively isolated from insulated joints (the closest is 42.8 m away) and other bridges. Then, the analysis of measurement speeds considers Bridge 3, as it has the largest speed variations from the measurement campaign (15.7 m/s and 24.2 m/s).

3.1. Multi-ABA responses at different wheelsets

Fig. 5 shows that signals from all the wheelsets provide strong responses at positions close to both abutments. For Bridge 6, the responses

Table 1
Railway bridge transition zones, aerial photographs, and side-view photographs (source of aerial photographs: BBMS, ProRail).

Transition Zone at Bridge #	Position (km)	Aerial Photo	Side-View Photos	
1	28.416 – 28.433	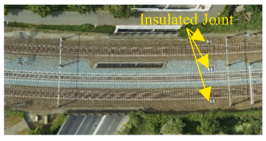		
2*	27.729 – 27.764	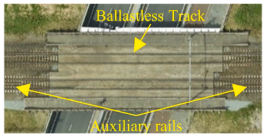		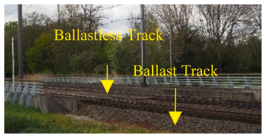
3	26.994 – 27.022	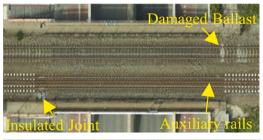		
4	25.256 – 25.265			
5	25.233 – 25.242			
6	24.652 – 24.661			
7*	17.835 – 18.940	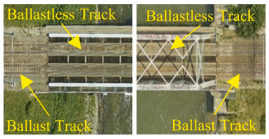	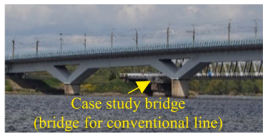	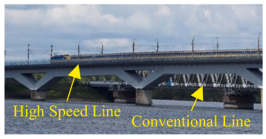
8	17.423 – 17.430	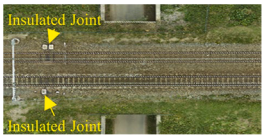		
9	17.270 – 17.297	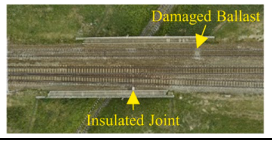		

Note: Bridges annotated with * contain ballastless track.

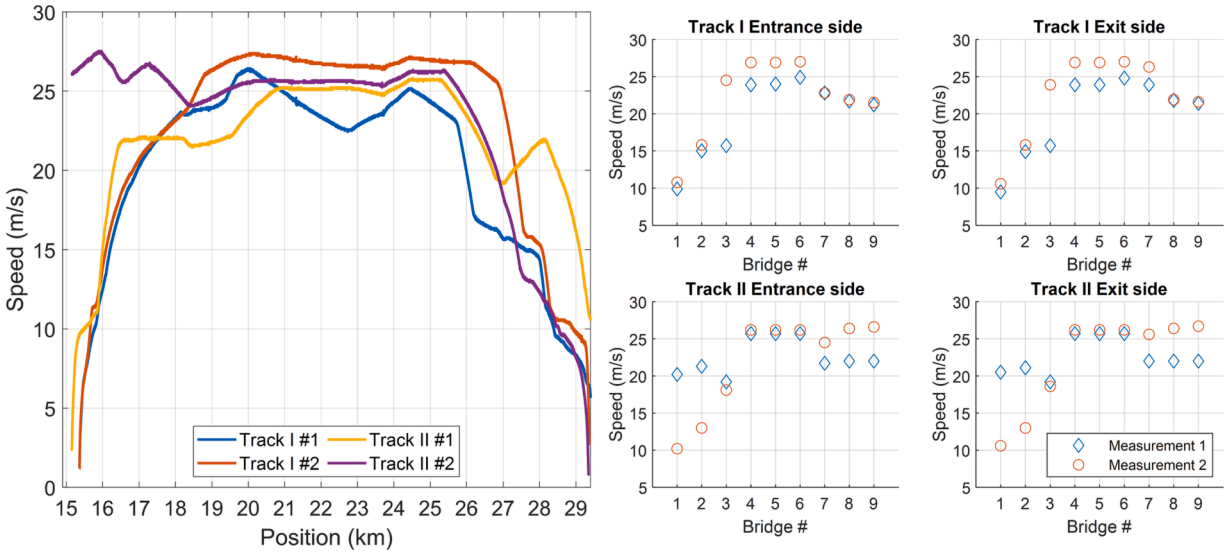

Fig. 4. Speed profile and average speed of the ABA measurement system at each transition zone from the measurement campaigns.

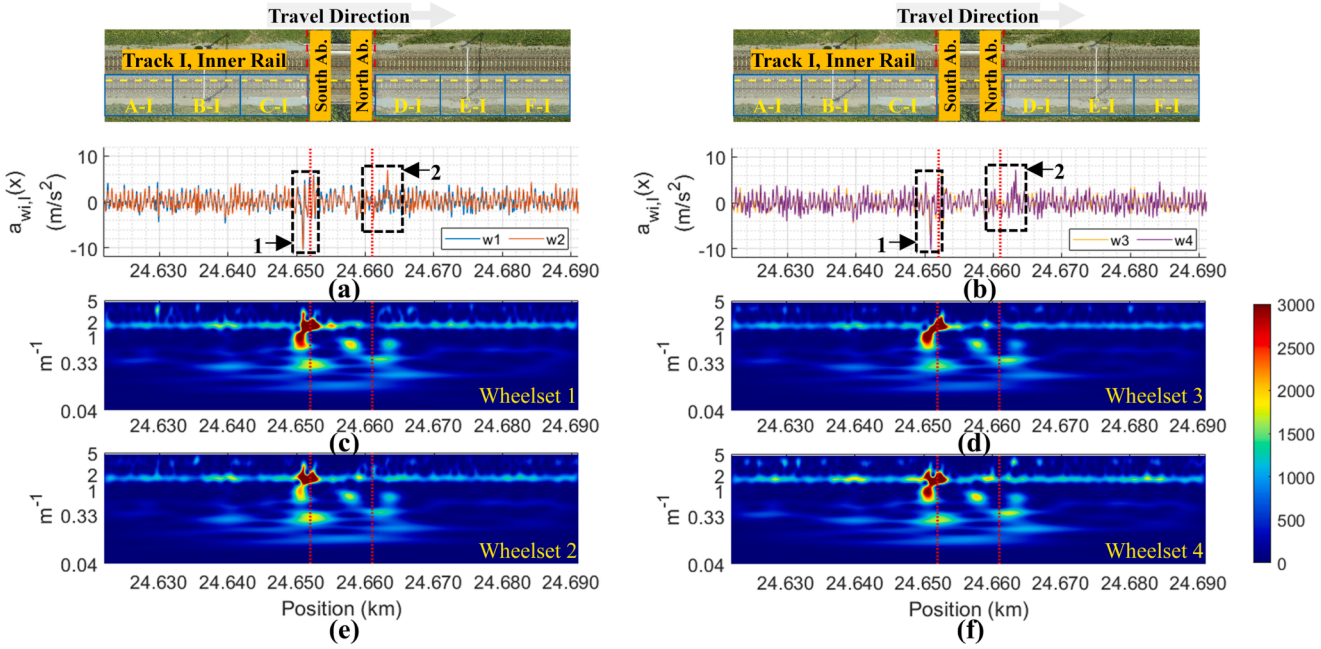

Fig. 5. Responses of the ABA signals from 4 wheelsets measured at the inner rail of Track I at Bridge 6, ABA signals with 100 Hz cutoff frequency (source of aerial photographs: BBMS, ProRail).

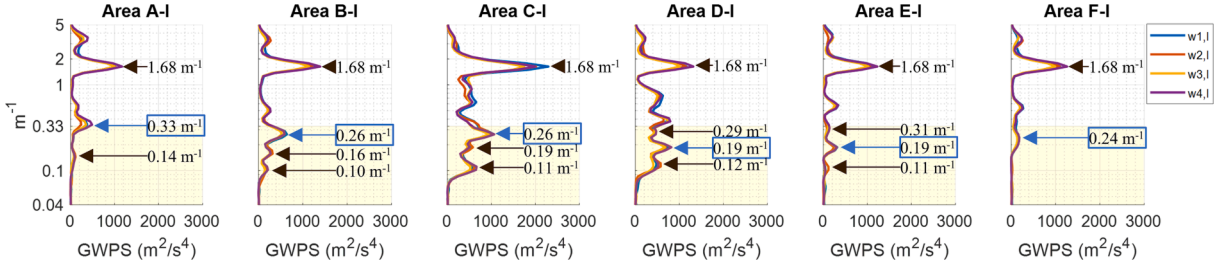

Fig. 6. GWPS of the ABA signals of the transition zones at the inner rail of Track I at Bridge 6. A-I to C-I are areas on the entrance side, and D-I to F-I are areas on the exit side.

near the South Abutment are stronger than the responses near the North Abutment. No indication of a significant difference in the wavelengths and amplitudes between the ABA signals measured from the four wheelsets is observed. Similar dominant peaks at the entrance and exit sides close to abutments are found from the four signals (see dashed rectangles 1 and 2 in Fig. 5(a) and (b)). Consequently, the WPS of the ABA signals from the four wheelsets follows similar patterns (see Fig. 5 (c), (d), (e), and (f)).

Fig. 6 shows that the GWPS responses from different wheelsets in each study area contain the same number of dominant peaks with slight amplitude differences. For Track I of Bridge 6, in the considered spatial frequency range from 0.04 m^{-1} to 0.33 m^{-1}, the closer the area is to the bridge, the higher the total energy. Furthermore, the dominant peak at each area varies in frequency and amplitude, as indicated by the blue rectangles in Fig. 6. Note the common peak outside the region of interest at 1.68 m^{-1}, which corresponds to a 0.60 m wavelength that is sleeper-related. This peak might be of interest for sleeper monitoring.

Fig. 7 presents the SAWP in the spatial frequency range from 0.04 m^{-1} to 0.33 m^{-1} from the four wheelsets. Although similar SAWP patterns are observed, differences are found in the peak locations and amplitudes. For example, the peaks in Area C-I have amplitudes between 0.48 m^2/s^4 and 0.67 m^2/s^4, and the positions of the peaks vary within a range of approximately 1 m. In the case of Area D-I, the peaks have amplitudes between 0.31 m^2/s^4 and 0.47 m^2/s^4 with less than 1 m variation in the position of the peaks.

Finally, different wheelsets provide similar responses when analyzing other transition zones. Thus, the average GWPS and SAWP can be considered to account for the minor variabilities between wheelset responses. Furthermore, we observed local changes in the spatial frequency range between 0.04 m^{-1} and 0.33 m^{-1} for different transition zones. Thus, the total energy of the SAWP is a good candidate for determining a general KPI for transition zones.

3.2. Influence of the measurement speed on multi-ABA responses

The influence of the measurement speed on multi-ABA responses is analyzed since the measurement speeds at different transition zones can vary due to different operational and track conditions. For Bridge 3, the ABA signal responses of wheelset 1 are shown in Fig. 8. The peak locations of the ABA signals are similar, but the amplitude of each peak is larger with a faster measurement speed (see Fig. 8(a) and (c)). Measurements at different speeds show different WPS and GWPS responses in terms of the energy level, but the locations of the corresponding dominant spatial frequencies are similar, as shown in Fig. 8(b), (d) and Fig. 9. We observe similar numbers of dominant peaks and notably alignment of peaks in all the different study areas (see yellow regions of Fig. 9). This shows good repeatability of the measurements. Furthermore, a comparison of the SAWP values of the ABA signals from the two measurement speeds is presented in Fig. 10. The result shows that a signal from a particular wheelset provides similar peak positions even though the measurement speeds are different. Moreover, the amplitude is larger with a faster measurement, and the differences are more prominent than with a slower measurement. Varying peak positions of approximately 1 m for different wheelsets are observed between measurements (as discussed in Section 3.1).

Finally, similar findings are obtained when analyzing other transition zones. That is, speed variations in the multi-ABA measurement have a minor influence on the location of the dominant peaks. However, the measurement speeds strongly influence the multi-ABA responses in terms of energy. As expected, faster speeds lead to larger dynamic responses of the train-track interactions [64]. The multi-ABA data characterize the responses of the whole track system under a very strong input excitation given by the moving load (train). This excitation is stronger than in conventional input excitation methods such as hammer tests and falling weight devices. The literature reports that substructure components dominate low frequencies, so a higher excitation of the substructure components is expected and provides a better estimation of their condition. For substructure condition assessment, a faster measurement speed is preferable in the design of KPIs for transition zones since it provides more noticeable responses due to the higher excitation level than a slower speed, particularly in the low-frequency range. Still, other track components are also more excited, necessitating further studies for separating the responses from each track component, for instance, from the subgrade, subballast, ballast, and sleepers.

4. Multi-ABA responses at different tracks and rails

The responses of multi-ABA signals measured at different tracks at the same bridge and different rails of the same track are investigated in this section. The multi-ABA signals measured at Bridge 6 are selected as an example since this bridge has the largest distance from other track components, such as insulated rail joints (see Fig. 11).

Additionally, signals with a minor difference in the measurement speeds between the two tracks are considered to reduce the speed effect on the analysis (as discussed in Section 3.2). Fig. 11 presents multi-ABA signals from the inner rail (I) and outer rail (O) for Tracks I and II in the space domain and their WPS values. The train moved with a speed of 24.9 m/s on Track I and 25.7 m/s on Track II. The responses from each rail and track show different energy distributions over the frequency range of interest. In the following subsections, we analyze these differences.

4.1. Responses of multi-ABA signals from different tracks

The sum of the SAWP values measured from the inner rail and outer rail for each of the four wheelsets is considered to study degradation at the track level. Fig. 12(a) and (b) show for Tracks I and II the averaged SAWP values from the four wheelsets and the interval defined by the

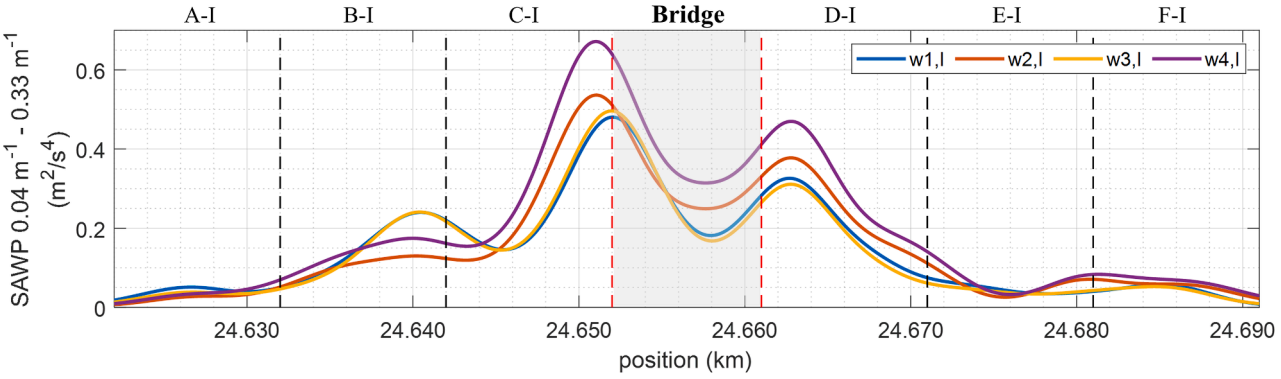

Fig. 7. SAWP of the ABA signals from 4 wheelsets at the inner rail of Track I at Bridge 6.

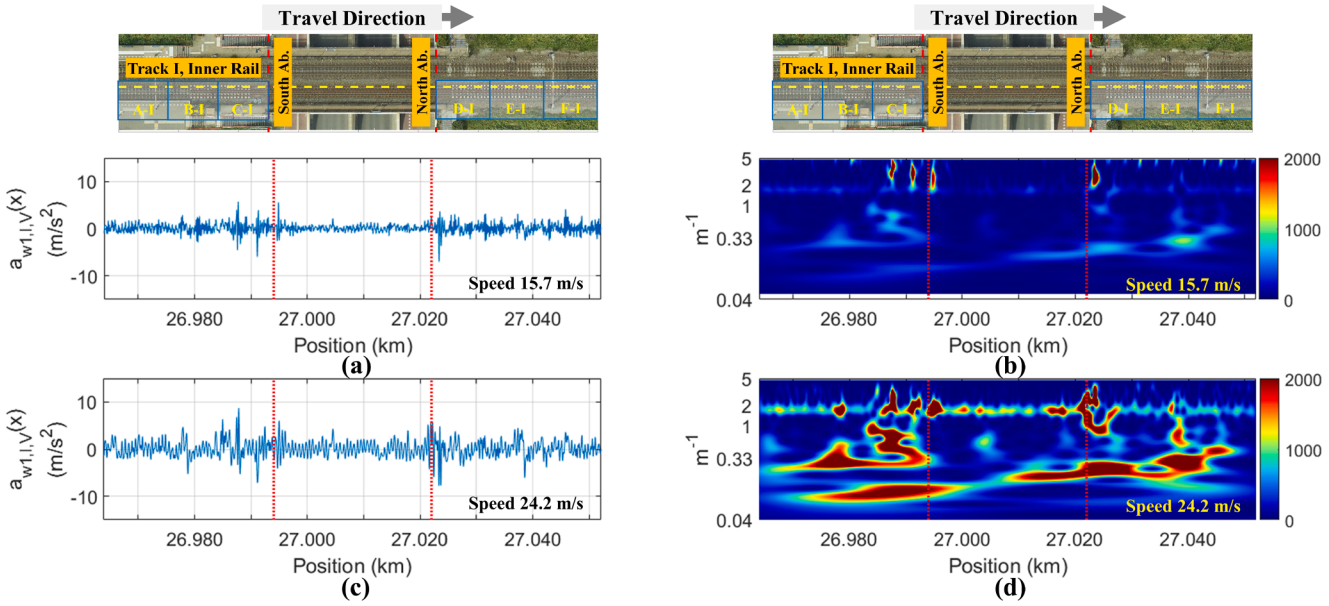

Fig. 8. ABA responses (with 100 Hz cutoff frequency) at Bridge 3 in wheelset 1 on the inner rail of Track I: (a) and (b) ABA and its WPS, measured at 15.7 m/s; and (c) and (d) ABA and its WPS, measured at 24.2 m/s (source of aerial photographs: BBMS, ProRail).

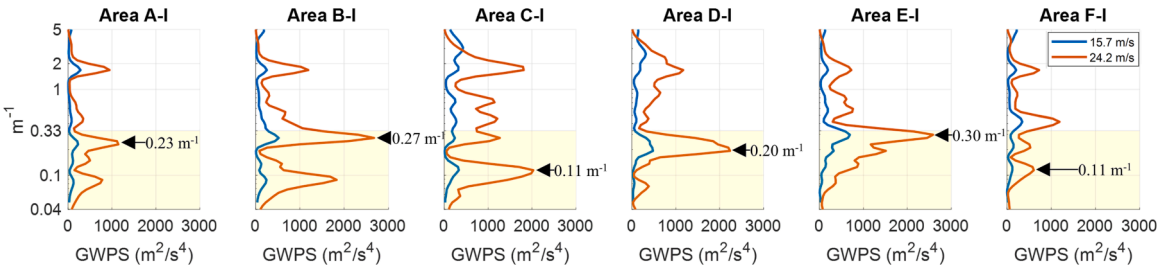

Fig. 9. GWPS of ABA signals from two different measurement speeds at Bridge 3 in wheelset 1 on the inner rail of Track I.

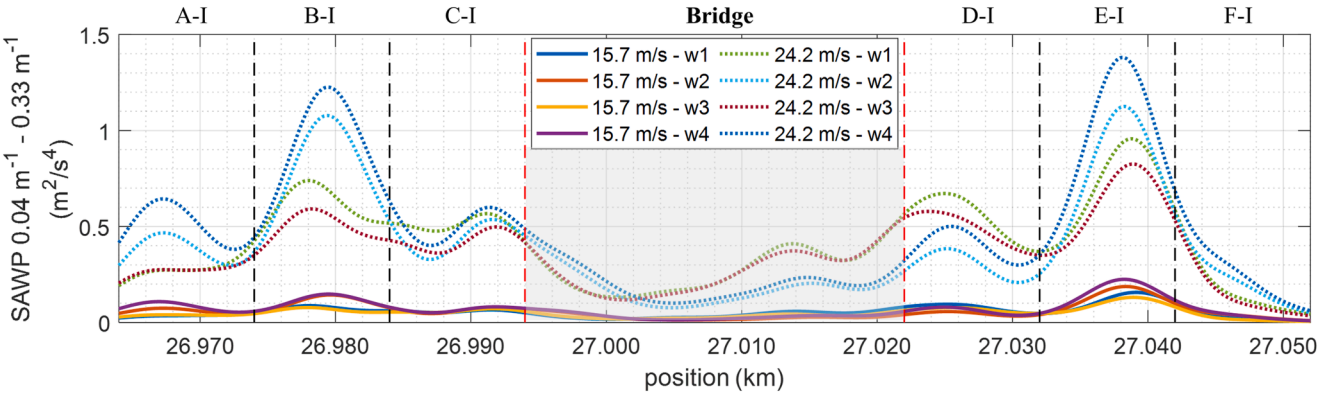

Fig. 10. SAWP of the ABA signals from two different measurement speeds at Bridge 3 for the inner rail of Track I.

maximum and minimum SAWP values, respectively. The results show that Track I exhibits unsmooth energy changes, with dips at kilometer 24.630 in Area A-I, kilometer 24.644 in Area C-I, and kilometer 24.676 in Area E-I (see Fig. 12(a)). The energy for Track II changes smoothly between consecutive study areas (see Fig. 12(b)), with no significant dips in Area A-II, Area C-II, and Area E-II, as observed in Area A-I, Area C-I and Area E-I. We do not observe local changes in Track II at kilometer positions of 24.630, 24.644, and 24.676. Additionally, there are no visible track components in Track I that explain the differences with Track II based on observations from the aerial photograph (see Table 1).

Next, in Fig. 13, the sum of SAWP values is used to quantify the amount of ABA energy in each study area. The results show that the sum of SAWP is higher for Track I in Areas A, B, and F. The ABA energy on the entrance side of Track I (Area C-I) is larger than that on the exit side (Area D-I) by 24.6%. Track II shows a smaller energy difference than Track I, for which the entrance side (Area C-II) energy is only 2.9% larger than that on the exit side (Area D-II). Fig. 13(c) shows the percentage of energy change between two consecutive study areas. The maximum percentage of change for Track I is 275.4% from Areas A-I to Area B-I, while the maximum change for Track II is 571.9% from Area B-

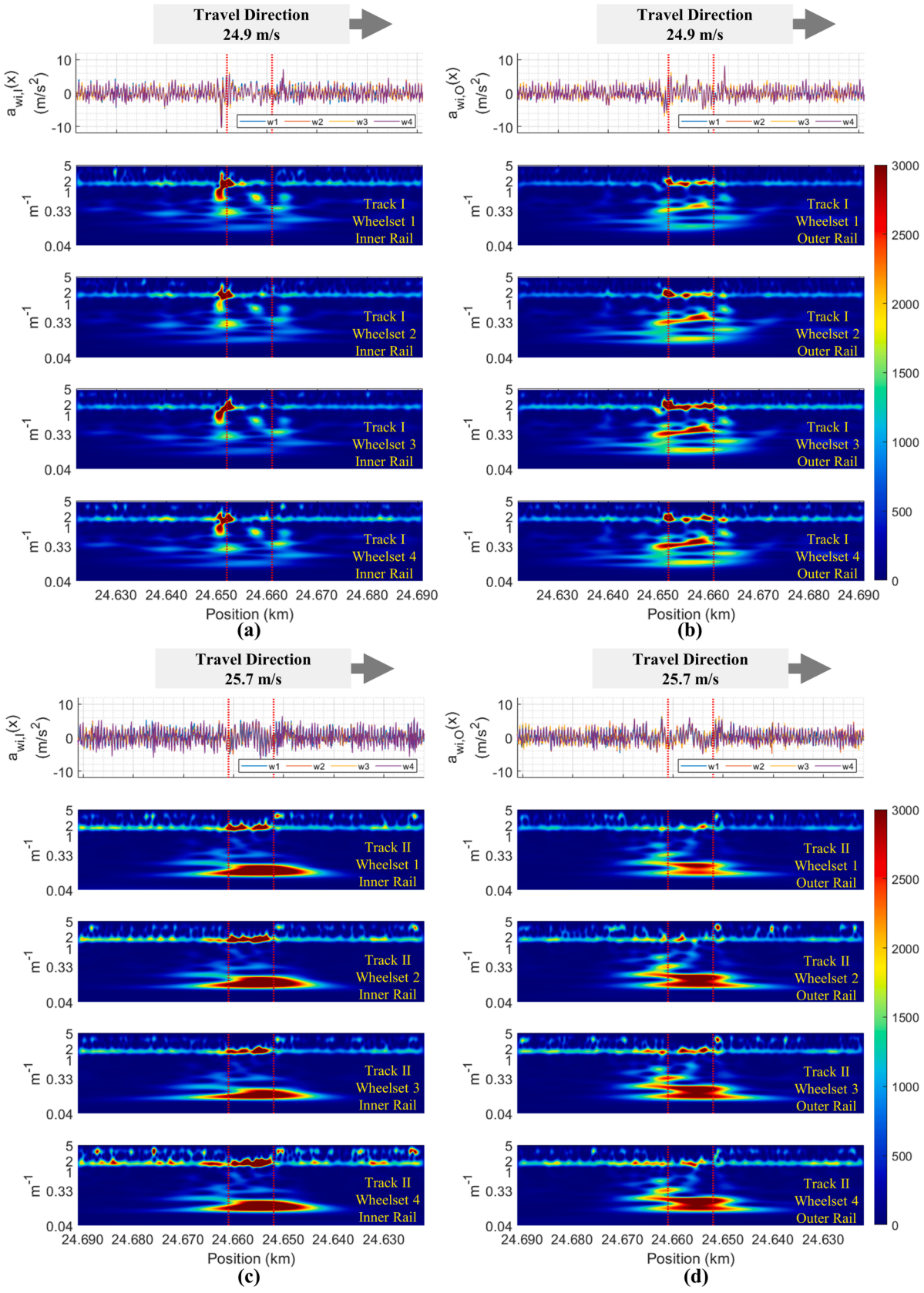

Fig. 11. Multi-ABA signals (with 100 Hz cutoff frequency) and WPS at Bridge 6: (a) signals for the inner rail of Track I, (b) signals for the outer rail of Track I, (c) signals for the inner rail of Track II, and (d) signals for the outer rail of Track II.

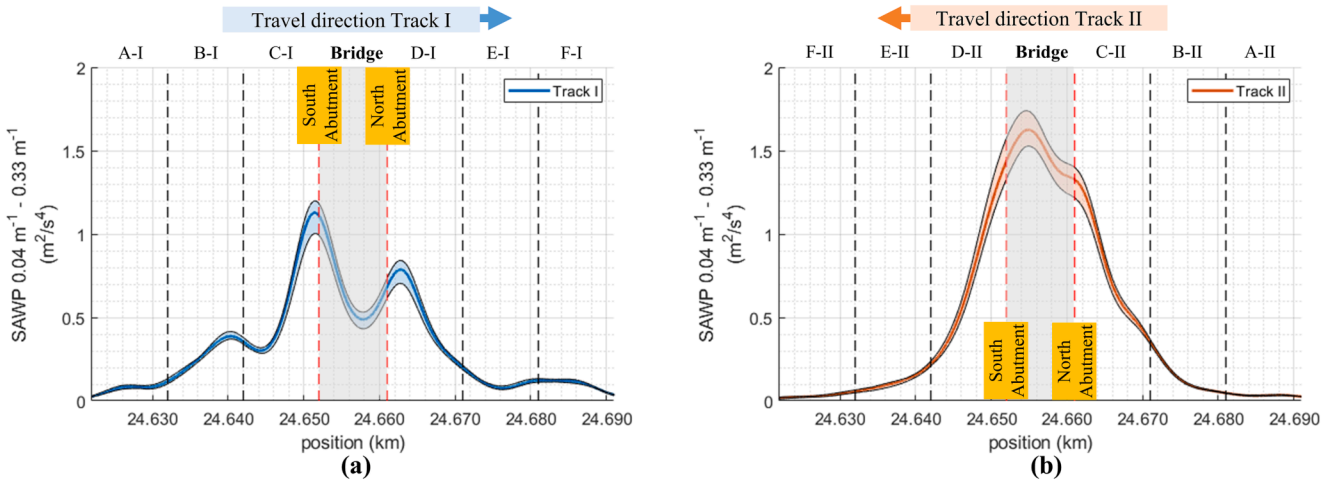

Fig. 12. SAWP of the two tracks at Bridge 6: (a) responses at Track I; (b) responses at Track II.

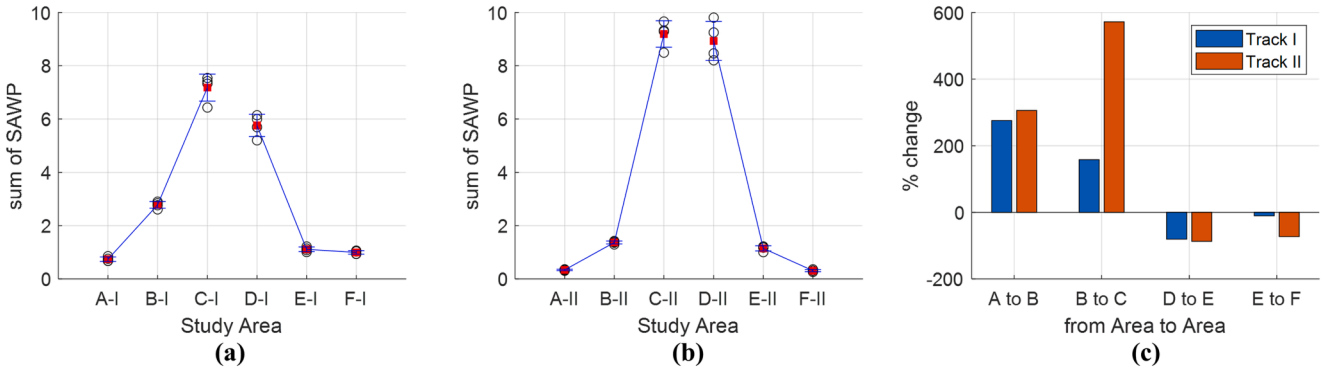

Fig. 13. Sum of SAWP values for different areas of Bridge 6:(a) study areas on Track I; (b) study areas on Track II; and (c) percentage of change between the study areas.

II to Area C-II. This finding suggests that the track components whose response is reflected in the range 0.04 m^{-1} to 0.33 m^{-1} (dominant by substructure [61–63]) in the studied transition zones for Track I and Track II are dissimilar. Further studies are needed to understand better the relation between the operational condition of the transition zones, multi-ABA signals, track geometry differences, and malfunctions at the

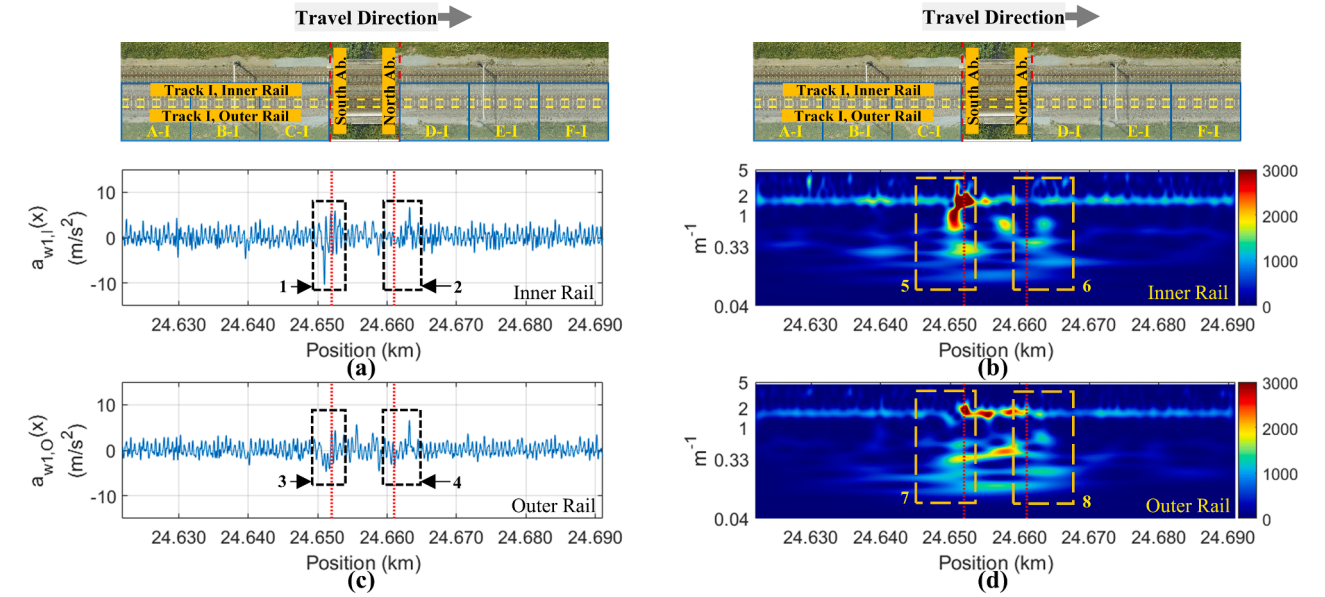

Fig. 14. ABA responses (with 100 Hz cutoff frequency) of Track I at Bridge 6: (a), (b) responses of the inner rail in the space domain and WPS; and (c), (d) responses of the outer rail in the space domain and WPS (source of aerial photographs: BBMS, ProRail).

track structure.

To compare abutments, the ABA energies in Areas C-I and D-II are summed to represent the conditions of the track segment near the South Abutment, which gives a value of 16.11 m^2/s^4. The sum of the ABA energy in Areas D-I and C-II represents the track segment near the North Abutment and is approximately 14.95 m^2/s^4. This calculation suggests that the South Abutment exhibits an approximately 7.8% higher energy than the North Abutment. Additional onsite investigations can provide a better understanding of these differences. For instance, a structural settlement or damages could be the possible reason to explain larger differences. Finally, when analyzing various bridges, the condition variation of the substructure at transition zones on the abutment level and track level is relatively local; for instance, the stronger degradation process of transition zones is not always located at the entrance side. This topic is discussed in Section 5.

4.2. Responses of multi-ABA signals from different rails

This section analyzes ABA signals from the inner rail (I) and outer rail (O). We use measurements from wheelset 1 in Bridge 6 as an example. Fig. 14(a) and (b) present the responses of the inner rail, while Fig. 14(c) and (d) show the outer rail responses. The ABA signals from the inner and outer rails yield similar peak positions (see blocks 1, 2, 3, and 4 in Fig. 14). However, the inner rail signal shows a significantly larger amplitude than the outer rail signal at a peak close to the South Abutment. This suggests that at Track I, the South Abutment experiences a stronger uneven degradation than the North Abutment. Consequently, the WPS values of the inner rail close to the South Abutment are significantly larger than those from the outer rail (see blocks 5 and 7).

Multi-ABA signals from both rails in terms of the GWPS values in each study area are compared in Fig. 15. Signals from the inner and outer rails show differences in the frequencies and amplitudes of the dominant peaks in the study areas. Areas C-I and D-I show noticeable response differences between the two rails in the spatial frequency range below 0.33 m^{-1} (see yellow regions). In addition, remarkable differences between the two rails are also found at spatial frequencies above 0.33 m^{-1} (see, for example, Area C-I). Even though the responses above 0.33 m^{-1} are not within the scope of this study, this finding could be indicative of transition zone health conditions related to the deterioration of sleepers, such as hanging sleepers. Hence, further studies are needed for a better understanding.

Next, the SAWP values of the signals at both rails in Tracks I and II and the corresponding track geometry parameters at the transition zones are shown in Fig. 16. Fig. 16(a) shows noticeable differences in Areas B-I, C-I, and D-I regarding the location and amplitude of the SAWP peak responses between the inner and outer rails. The inner rail shows larger energies than the outer rail in Area B-I, while the outer rail shows larger energies in Areas C-I and D-I. The responses of Track II in Fig. 16(b) show significantly different responses in Area C-II (outer rail with higher energy) and Area D-II (inner rail with higher energy). These findings suggest a sensitivity of the multi-ABA to estimate responses from signals measured at different rails. While slight amplitude variations, and similar peaks and wave behavior can be observed. A possible reason to explain this higher spatial resolution is that the multi-ABA measures 25,600 times in a second (or every 1.5 mm) when the measurement speed is 140 km/h. In the case of conventional track geometry recording car, the signals are reported every 25 cm.

Although the ABA measurement system can detect differences in ABA energy between 2 rails, current substructure remedies in practice, for instance, ballast tamping and subgrade strengthening, are mainly conducted underneath two rails simultaneously. Nevertheless, this detection capability might provide indications to support track substructure maintenance solutions at specific spots with next-generation technology. Furthermore, numerical simulations of the transition zones can be developed and fine-tuned to reproduce this effect, and then we can expect a better understanding of the track parameters. Furthermore, we found a considerable variation in track geometry parameters, especially in Area C and Area D on both tracks, where the SAWPs also vary significantly. This finding might relate to the reported relationship between the longitudinal level and the track substructure conditions [62,72–76]. Since in this paper we consider the various layers of the substructure as a whole, a determination of the severity level of each layer is required for a more detailed maintenance planning. Therefore, further studies could support a better understanding of the relationship between ABA signals and track geometry parameters, making track substructure condition assessment more informative and insightful.

5. Key performance indicators based on the Multi-ABA for transition zones

This section proposes a methodology for continuously monitoring the degradation levels of transition zones using KPIs based on multi-ABA measurements. Previous studies reported that more severe degradation levels of track components provide larger ABA energies [57,58]. Assuming that an undegraded condition has the lowest percentage of energy contents, a large difference between the energy contents of the two transition zones indicates that the transition zone with high energy content should have a more severe degradation. Therefore, the relative percentage difference of the energy content is proposed as an indicator of transition zone health conditions. Thus, ABA energy-based KPIs are developed to evaluate differences between transition zones using SAWP. At a particular bridge, four KPI types are proposed in this study to represent an ABA energy comparison of transition zones at different abutments (North and South), tracks (I and II), sides (entrance and exit), and rails (inner and outer). A brief description of a particular KPI is shown in Table 2. Since we discussed in the previous sections that the ABA energy is highly location- and speed-dependent, measurements with minor speed differences between Tracks I and II are selected.

5.1. KPI for abutments

As discussed in Section 4.1, the SAWP sum at Area C-I of Track I and Area D-II of Track II can be used to represent the condition of track segments associated with the South Abutment, while the SAWP sum at

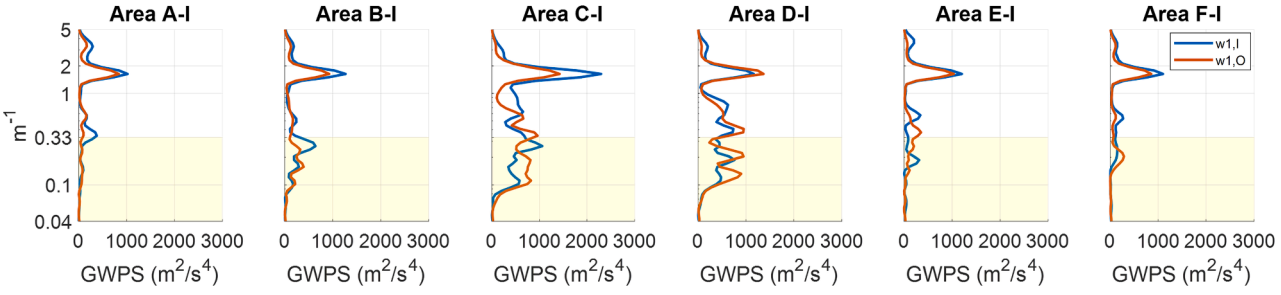

Fig. 15. GWPS of the ABA signals measured at different rails for Track I at Bridge 6.

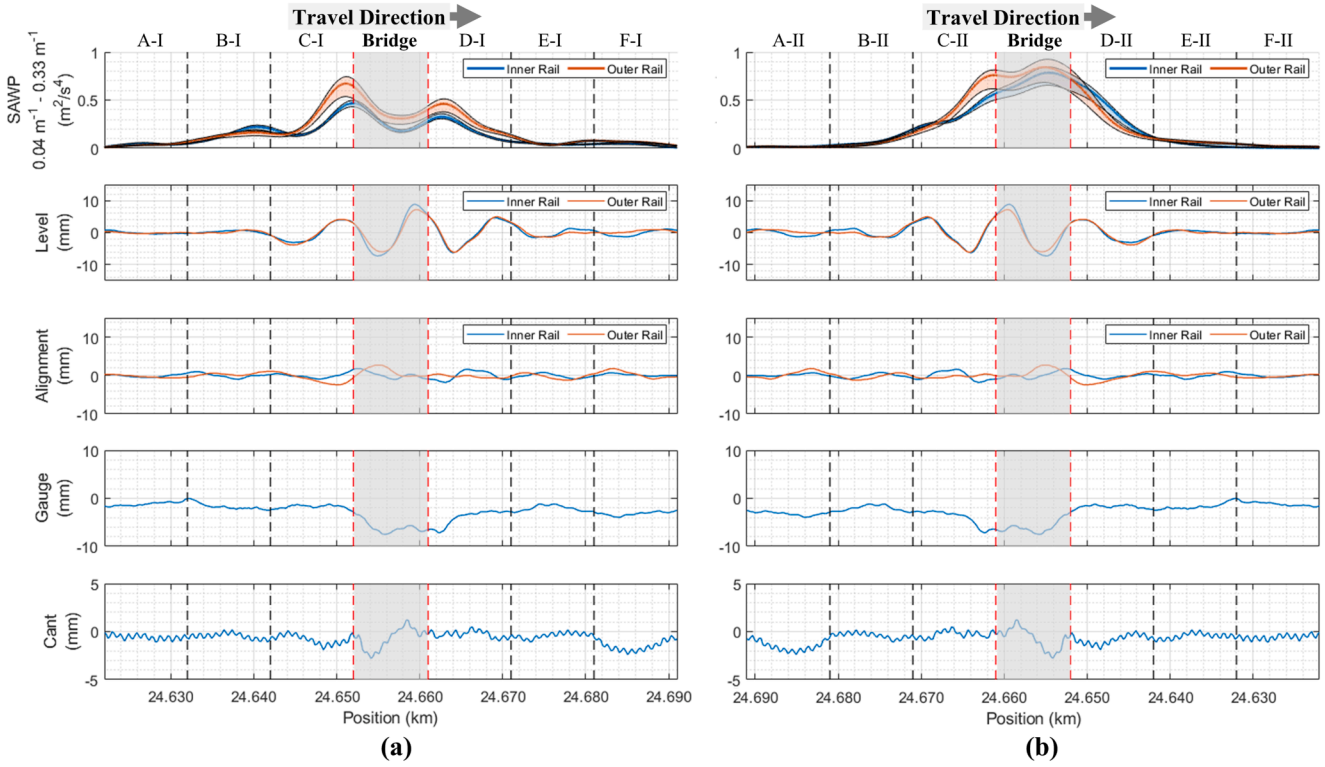

Fig. 16. SAWP of the ABA signals and track geometries at Bridge 6: (a) measurement for Track I and (b) measurement for Track II.

Table 2
Description of the proposed KPIs.

KPIs	Description
$KPI_b^{abutment}$	Relative energy difference between the South and North Abutments at bridge *b*.
$KPI_{b,a}^{track}$	Relative energy difference between 2 tracks that is associated with abutment *a* (either the South or the North Abutment) of bridge *b*.
$KPI_{b,t}^{side}$	Relative energy difference between the entrance and exit sides of track *t* (either Track I or Track II) of bridge *b*.
$KPI_{b,s,t}^{rail}$	Relative energy difference between the inner and outer rails of side *s* (either the entrance side or exit side) of track *t* of bridge *b*.

Areas D-I and C-II can be used to represent track segments that correspond to the North Abutment. Therefore, a KPI for evaluating differences in degradation level between abutments is proposed as follows:

$$KPI_b^{abutment} = \frac{\left(\sum_{x=x_3}^{x_4} \overline{SAWP}_b^{\text{Track I}}(x) + \sum_{x=x_3}^{x_4} \overline{SAWP}_b^{\text{Track II}}(x)\right) - \left(\sum_{x=x_1}^{x_2} \overline{SAWP}_b^{\text{Track I}}(x) + \sum_{x=x_1}^{x_2} \overline{SAWP}_b^{\text{Track II}}(x)\right)}{\frac{\left(\sum_{x=x_3}^{x_4} \overline{SAWP}_b^{\text{Track I}}(x) + \sum_{x=x_3}^{x_4} \overline{SAWP}_b^{\text{Track II}}(x)\right) + \left(\sum_{x=x_1}^{x_2} \overline{SAWP}_b^{\text{Track I}}(x) + \sum_{x=x_1}^{x_2} \overline{SAWP}_b^{\text{Track II}}(x)\right)}{2}} \times 100 \quad (6)$$

where *b* is the bridge number, $\sum_{x=x_m}^{x_n} \overline{SAWP}_b^{\text{Location}}(x)$ is the ABA energy at a considered location from kilometer x_m to x_n, $\overline{SAWP}_b(x)$ is an averaged SAWP from 4 wheelsets, x_1 and x_2 are kilometer positions defining the South Abutment (Areas C-I and D-II), and x_3 and x_4 define the North Abutment (Areas C-II and D-I). According to (6), a negative $KPI_b^{abutment}$ indicates that the transition zones associated with the South Abutment are more degraded, and a positive $KPI_b^{abutment}$ indicates that the transition zones associated with the North Abutment are more degraded. Values of approximately 0% represent cases when the ABA energy contents (as associated with degradation conditions) between the transition zones at the South and North Abutments are similar.

Fig. 17(a) shows the partition of the total ABA energy content between the South and North Abutments, and Fig. 17(b) shows $KPI_b^{abutment}$. The KPI ranges from −79.7% to 92.4% for the bridges in the case study. In 4 out of 9 bridges (bridges 1, 3, 4, and 8), more severe degradation occurs at the North Abutment. Furthermore, three bridges indicate a considerable difference, approximately 80.0%: $KPI_2^{abutment}$ is −79.4%, $KPI_3^{abutment}$ is 92.4% and $KPI_4^{abutment}$ is 78.0%. Finally, Fig. 17(a) and (b) show that the degradation level of the track segments associated with two abutments can vary and that each bridge exhibits individual degradation characteristics reflected by the KPI.

5.2. KPI for tracks

At a particular abutment, we define a KPI that estimates the difference in the ABA energy between different tracks. This KPI is defined as follows:

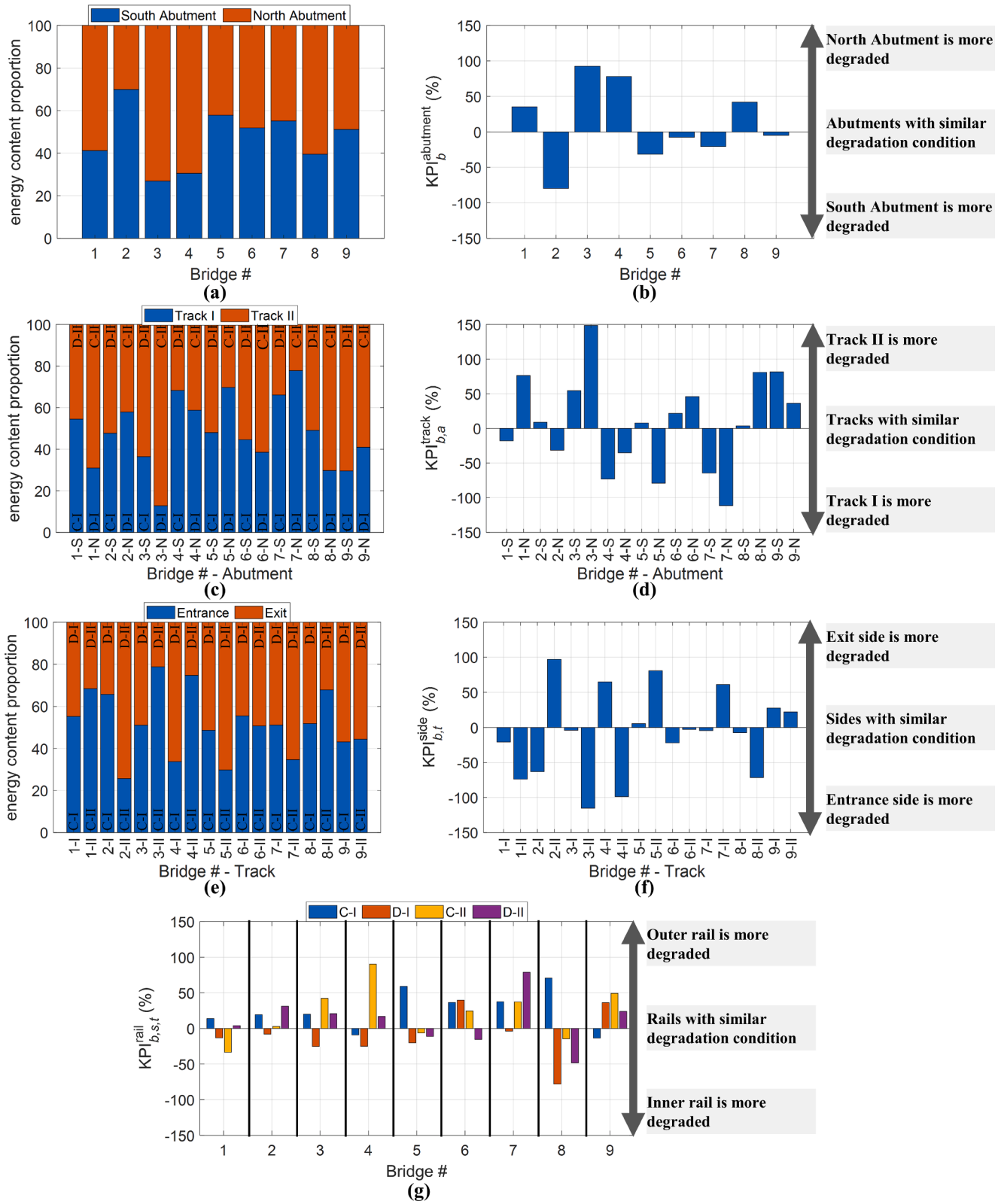

Fig. 17. Degradation level evaluation at different locations of transition zones: (a), (c), (e) partition of total energy content between the two abutments, two tracks at a particular abutment, two sides at a particular track; (b), (d), (f), (g) KPI to evaluate substructure condition differences between abutments, tracks, sides, and rails.

$$\mathrm{KPI}_{b,a}^{\mathrm{track}} = \frac{\left(\sum_{x=x_m}^{x_n} \overline{SAWP}_{b,a}^{\mathrm{Track\ II}}(x) - \sum_{x=x_m}^{x_n} \overline{SAWP}_{b,a}^{\mathrm{Track\ I}}(x)\right)}{\frac{\left(\sum_{x=x_m}^{x_n} \overline{SAWP}_{b,a}^{\mathrm{Track\ II}}(x) + \sum_{x=x_m}^{x_n} \overline{SAWP}_{b,a}^{\mathrm{Track\ I}}(x)\right)}{2}} \times 100 \tag{7}$$

where b is the bridge number, a is either S (South Abutment) or N (North Abutment), $\sum_{x=x_m}^{x_n} \overline{SAWP}_{b,a}^{\mathrm{Location}}(x)$ is the ABA energy from kilometer x_m to x_n at Abutment a, and $\overline{SAWP}_{b,a}(x)$ is an averaged SAWP from 4 wheelsets. According to (7), at any abutment, positive value of $\mathrm{KPI}_{b,a}^{\mathrm{track}}$

indicates that Track II is degraded more, and negative $KPI_{b,a}^{track}$ indicates that Track I is degraded more. Values of approximately 0% suggest that both tracks have a similar degradation condition at the abutment.

Fig. 17(c) shows the partition of total ABA energy content between Tracks I and II for each abutment in the case study. These results show that the ABA energy is distributed differently at each abutment. Fig. 17 (d) shows $KPI_{b,a}^{track}$ for all the abutments of the case study. The results from 18 abutments show that positive KPI values are found in 11 abutments (in the ranges from 3.7% to 148.6%), and negative values in 7 abutments are found (from −17.9% to −111.3%). Moreover, 2 out of 18 abutments provide the highest differences between tracks (>100.0%). The North Abutment of Bridge 3 exhibits a higher degradation of Track II, and the North Abutment of Bridge 7 shows a higher degradation of Track I.

5.3. KPI for the exit and entrance sides

A KPI is designed to quantify the degradation differences between the entrance side at Area C and the exit side at Area D of a particular track. This KPI for evaluating differences between the exit and entrance sides of a track is:

$$KPI_{b,t}^{side} = \frac{\left(\sum_{x=x_3}^{x_4} \overline{SAWP}_{b,t}^{exit}(x) - \sum_{x=x_1}^{x_2} \overline{SAWP}_{b,t}^{entrance}(x)\right)}{\frac{\left(\sum_{x=x_3}^{x_4} \overline{SAWP}_{b,t}^{exit}(x) + \sum_{x=x_1}^{x_2} \overline{SAWP}_{b,t}^{entrance}(x)\right)}{2}} \times 100 \quad (8)$$

where b is the bridge number, t is either I or II referring to Track I or Track II, respectively, $\sum_{x=x_m}^{x_n} \overline{SAWP}_{b,t}^{location}(x)$ is the ABA energy at a considered location from kilometer x_m to x_n, $\overline{SAWP}_{b,t}(x)$ is an averaged SAWP from 4 wheelsets, x_1 and x_2 are the kilometer positions of the entrance side (Area C), and x_3 and x_4 are the kilometer positions of the exit side (Area D). According to (8), a negative $KPI_{b,t}^{side}$ indicates that the entrance side is degraded more, and a positive $KPI_{b,t}^{side}$ indicates that the exit side is degraded more. Values near 0% indicate similar degradation conditions on both sides.

Fig. 17(e) shows the partition of total ABA energy between the entrance and exit sides, and Fig. 17(f) shows $KPI_{b,t}^{side}$ for all the case study locations. In 7 cases, the exit side is more degraded, with KPI values ranging from 5.5% to 97.0%. In 11 cases, the entrance side is more degraded, with KPI values from −2.9% to −115.3%. Finally, Track II of Bridge 2 shows the highest positive value (97.0%), and Track II of Bridge 3 and Track II of Bridge 4 provide the most negative values (−115.3% and −99.0%, respectively). Fig. 17(e) and (f) indicate that the degradation severity is related to the local condition of the track.

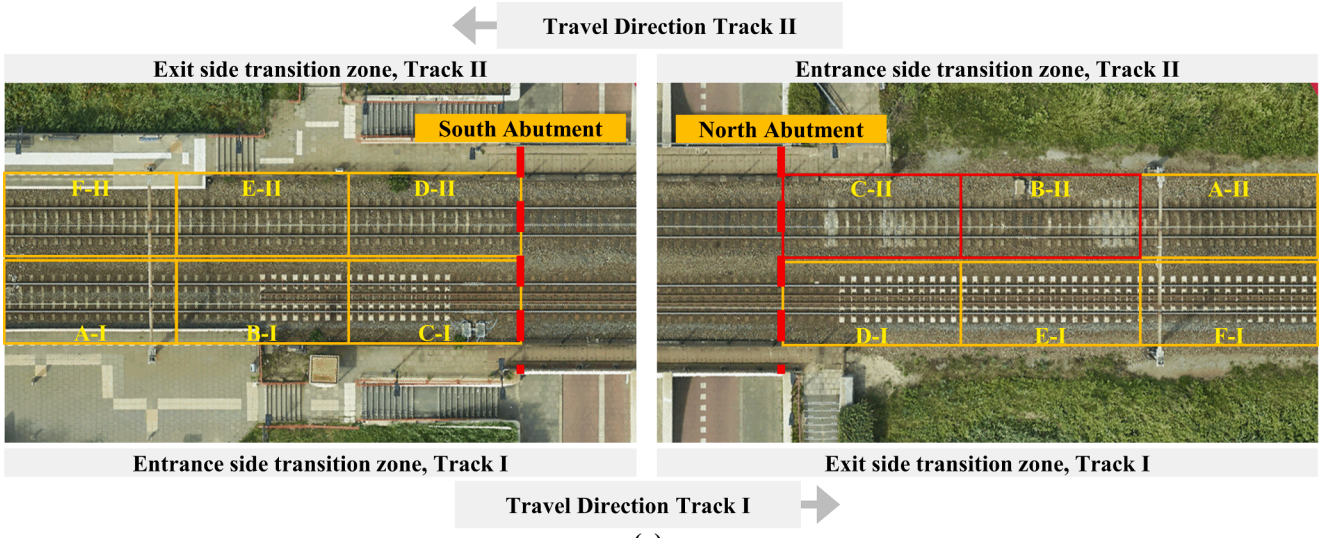

Fig. 18. Photos of Bridge 3: (a) aerial photographs, where the red rectangle indicates the different appearances of ballast at the entrance site of Track II; (b) site visit photographs taken at the entrance side of Track II (source of aerial photographs: BBMS, ProRail).

Fig. 18 shows aerial photographs taken in 2019 and site-visit photographs taken in 2021 at Track II of Bridge 3, which has the highest negative KPI value. The photographs show remarkable differences in the ballast appearance at the entrance side of Track II, especially in Areas B-II and C-II. The site-visit photograph shows that some new ballast has been placed. The images suggest that the area has required various maintenance interventions in the last few years. The KPI suggests that the problem is substructure-related.

5.4. KPI for inner and outer rails

Following the discussion in Section 4.2, we propose quantifying the local differences between the inner and outer rails at the transition zones of each bridge, side, and track. This KPI is defined as follows:

$$\mathrm{KPI}^{\mathrm{rail}}_{b,s,t} = \frac{\left(\sum_{x=x_m}^{x_n} \overline{SAWP}^{\mathrm{outer}}_{b,s,t}(x) - \sum_{x=x_m}^{x_n} \overline{SAWP}^{\mathrm{inner}}_{b,s,t}(x)\right)}{\frac{\left(\sum_{x=x_m}^{x_n} \overline{SAWP}^{\mathrm{outer}}_{b,s,t}(x) + \sum_{x=x_m}^{x_n} \overline{SAWP}^{\mathrm{inner}}_{b,s,t}(x)\right)}{2}} \times 100 \quad (9)$$

where b is the bridge number, s is either C or D referring to Area C (entrance area) or Area D (exit area), respectively, t is either I or II referring to Track I or Track II, respectively, $\sum_{x=x_m}^{x_n} \overline{SAWP}^{\mathrm{location}}_{b,s,t}(x)$ is the ABA energy at a considered location from kilometer x_m to x_n, and $\overline{SAWP}^{r}_{b,s,t}(x)$ is an averaged SAWP from 4 wheelsets, where r is either the inner or outer rail. According to (9), $\mathrm{KPI}^{\mathrm{rail}}_{b,s,t}$ is negative when the signals suggest greater degradation of the inner rail, and $\mathrm{KPI}^{\mathrm{rail}}_{b,s,t}$ is positive for greater degradation of the outer rail.

Fig. 17(g) shows $\mathrm{KPI}^{\mathrm{rail}}_{b,s,t}$ for the case study. In 21 out of 36 sides, a positive KPI value from 2.8% to 90.2% is found, indicating that ABA signals from the inner rail suggest a less severe degradation than in the outer rail. In the remaining 15 tracks, negative KPI values from −4.0% to −78.1% indicate a higher degradation from the inner rail signals. Furthermore, most of the differences range from −40.0% to 40.0%, with only three cases providing considerable differences of approximately 80.0% or higher. The entrance side at Track II of Bridge 4 and the exit side at Track II of Bridge 7 show the most positive KPI values of 90.2% and 78.8%, respectively. The exit side at Track I of Bridge 8 provides the most negative KPI value at −78.1%.

The finding shows that the degradation differences between the two rails are not detectable in most cases. Regarding the findings of this section, the locations that show higher degradation levels could be further investigated to identify the causes and effects on the performance of the transition zones. Consequently, tailored maintenance planning with suitable track remedies can be performed at those specific locations.

6. Evolution of KPIs over time

This section analyzes the evolution of the KPIs over time at transition zones. The datasets of ABA signals from measurement campaigns in 2016, 2019 (the dataset used in Section 5), and 2022 are used as primary inputs for this analysis. Since track maintenance records are unavailable, we use the track geometry parameters from 2016 to 2022 to calculate the track quality index. In this study, we use combined standard deviation (CoSD), according to EN 13848–6, which is proposed as follows:

$$CoSD = \sqrt{w_{\overline{AL}} SD^2_{\overline{AL}} + w_G SD^2_G + w_C SD^2_C + w_{\overline{LL}} SD^2_{\overline{LL}}} \quad (10)$$

where SD_i is the standard deviation of the individual geometry parameter i, w_i is the weighting factor of the individual geometry parameter i (set in this study at 0.25 for each parameter). $\overline{AL}$ is the average alignment of the inner and outer rails, G is the track gauge, C is the cant, and $\overline{LL}$ is the average longitudinal level between 2 rails. Since the data over time for Bridge 9 is unavailable, the analysis in this section considers Bridges 1–8. Fig. 19 shows the variation of track quality in terms of CoSD over time. The track quality of the transition zone at Bridge 3 on Track II

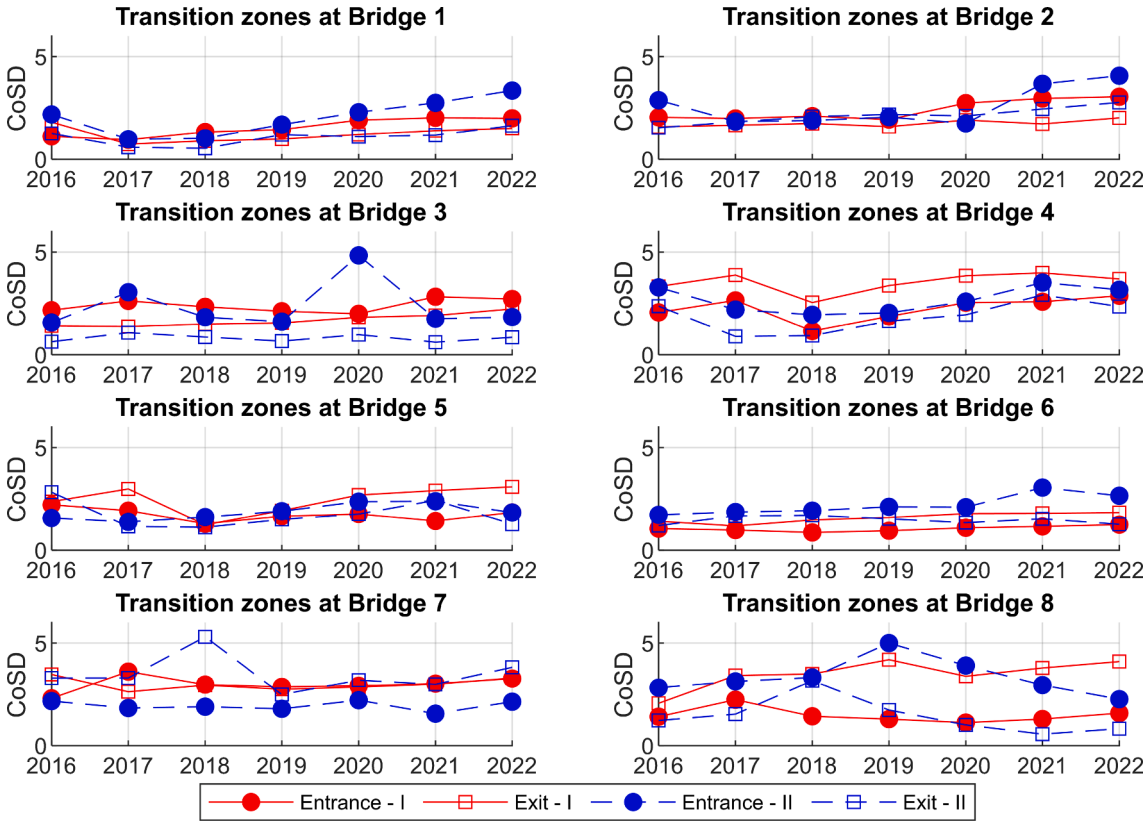

Fig. 19. Track quality at transition zones from 2016 to 2022.

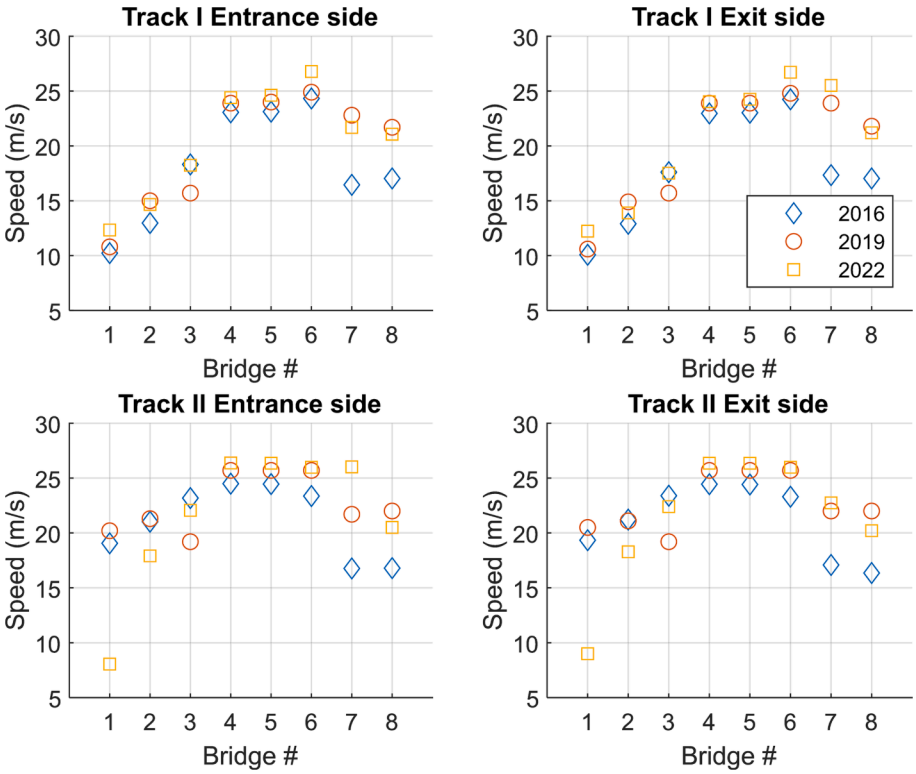

Fig. 20. Speed differences at a particular transition.

at the entrance side significantly dropped from 2020 to 2021. This finding agrees with observations from track visits in 2021, indicating that new ballast was placed, as shown in Fig. 18.

The ABA energy is speed-dependent, and there are differences in the measurement speed between years at a particular transition zone, as shown in Fig. 20. To examine the usefulness of the sum of SAWPs as a KPI input, we selected transition zones at Bridge 4, Track I, since this location was measured with the most similar speeds between years (with differences ranging from 0.1 m/s to 1.3 m/s).

Fig. 21(a) shows the SAWP evolution over time. Then, the sum of SAWPs at zones C and D are calculated and shown in Fig. 21(b) and (c), respectively. The results show that the conditions of both transition zones at the entrance and exit sides in 2016 were more degraded than in 2019 since a lower measurement speed provided higher ABA energy. The measurement speed in 2019 is 3.91% higher than speed in 2016, while ABA energy in 2019 of the entrance and exit sides is lower than in 2016 by 43.83% and 45.74%, respectively. This finding is consistent with the change in track quality over time as shown in Fig. 19 since indications of maintenance activities appeared in 2018. With the same criteria, we can conclude that transition zone conditions in 2022 were more degraded than in 2016 and 2019 because of a higher ABA energy. Note that the speed in 2022 is slightly higher than in previous years. The measurement speed in 2022 is 5.22% higher than in 2016 and 1.25% higher than in 2019. For the entrance side, the ABA energy in 2022 is 168.50% higher than in 2016 and 378.04% higher than in 2019. For the exit side, the ABA energy in 2022 is 24.09% higher than in 2016 and 128.69% higher than in 2019.

Fig. 21(d) shows the KPI for the entrance and exit side transition zones at bridge 4 ($KPI_{4,I}^{side}$). In 2016, the transition zone on the exit side was 69% more degraded than that of the entrance side. Then, this difference decreased to 66% in 2019, and finally, the entrance side transition zone was 5.4% more degraded than the exit side one in 2022. This finding suggests that the proposed KPI can represent the degradation evolution of transition zones.

Fig. 22 shows $KPI_{b,t}^{side}$ over time. The most dramatic change in the health condition, a 121.5% increase, occurred at transition zones at Bridge 2, Track II. The exit side transition zone was more degraded than the entrance side by 99.0% in 2019. Then, in 2022, the transition zone at the entrance side was more degraded than the exit side by 22.5%. In contrast, a minor change, 1.7%, occurred at the transition zones at Bridge 4, Track I. Additional sources of measurement data and onsite investigations are needed for a better understanding of the degradation mechanism of transition zones and to relate KPIs with malfunction causes.

Another KPI that can be evaluated for transition zones is by considering the vibration acceleration level (VAL), defined as [77]:

$$VAL(f_i) = 20\log_{10}\left(\frac{a(f_i)}{a_0}\right) \tag{11}$$

where $a(f_i)$ is the root mean square of the acceleration at the 1/3 octave band center frequency f_i, a_0 is the reference acceleration, which is 10^{-6} m/s^2.

In this study, when calculating the VAL at a specific section, the ABA signals are considered on the track level, including two rails. The VAL at the conventional track (30 m before the entrance transition zone) and at the entrance side transition zone (30 m before the entrance abutment) of Bridge 6 is shown as an example in Fig. 23. The results show that in the considered spatial frequency range of 0.04 m^{-1} to 0.33 m^{-1} (substructure related), the VAL of the conventional track is about 100 dB or lower, which is significantly lower than the level of the transition zone where the VAL is in between 100 dB and 110 dB. According to the VAL, the example transition zone provides a vibration 10 times higher than the nearby conventional track. This finding agrees with the 1/3 octave band spectra of the longitudinal level in Fig. 24. The transition zone provides substructure-related geometry variance 10 times higher than the conventional track. The VAL of the longitudinal level of the conventional track is in the range of 100–110 dB, while that of the transition zone is in the range of 110–120 dB.

The above-mentioned finding supports that the VAL (1/3 octave band spectra) can also be adopted as a KPI. Fig. 24 shows the evolution

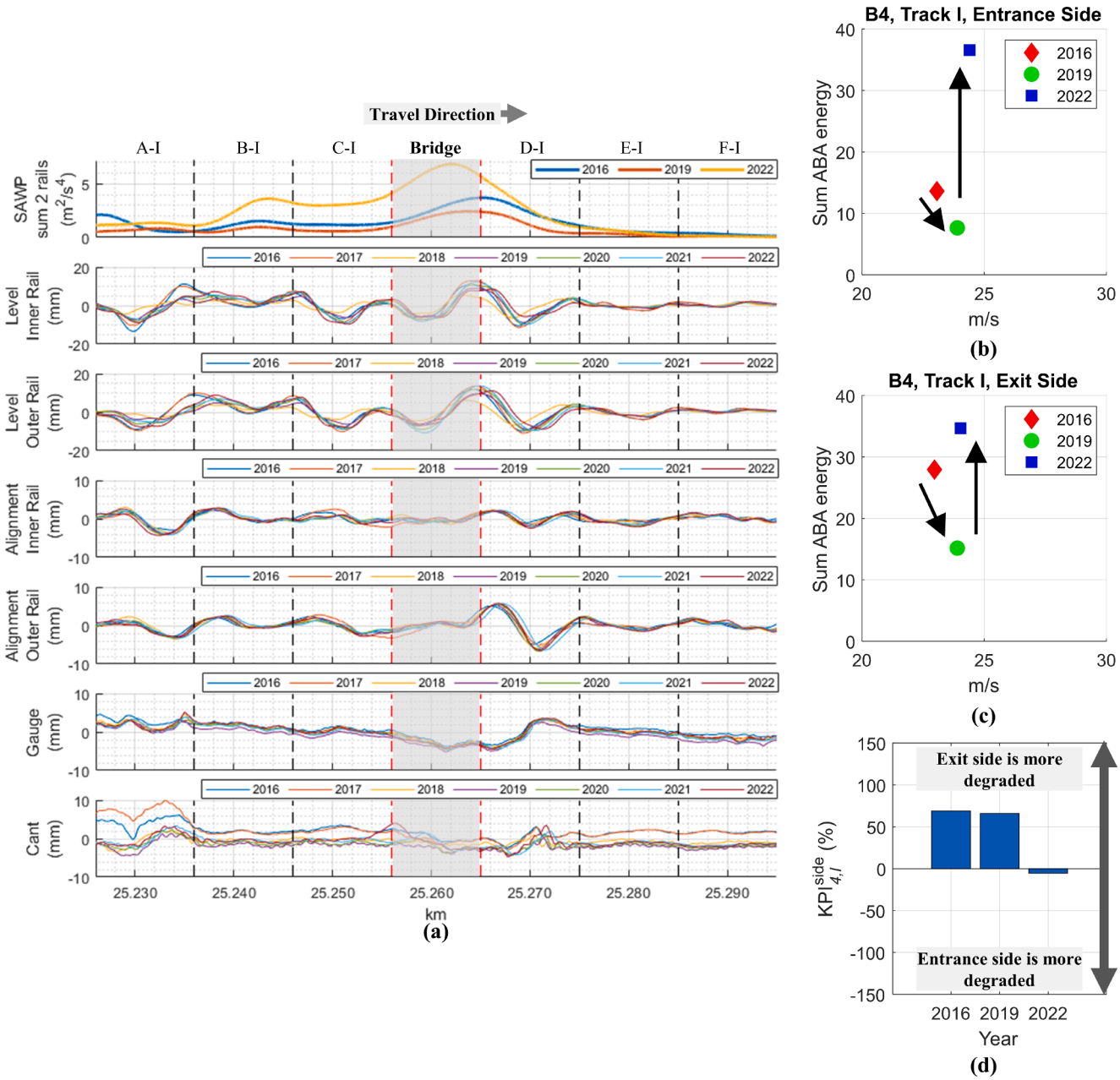

Fig. 21. Evolution of transition zones degradation at Bridge 4, Track I: (a) SAWP curves and track geometry parameters over time; (b),(c) comparison of ABA energy at entrance side and exit side transition zones; (d) KPI to evaluate condition differences between sides.

of VAL at the entrance transition zone of Bridge 4 (same bridge as in Fig. 21). The finding shows that the condition in 2022 is more severe than in 2016 and 2019 since the VAL amplitudes in the substructure-related ranges are higher than in other years. The findings from VAL shows good agreement with the analysis results from the SAWP quantity, as shown in Fig. 21.

Fig. 25 shows that the 1/3 octave band, PSD, and GWPS provide similar information on the distribution of ABA energy in the frequency domain. Since ABA signals are non-stationary, the frequency domain quantities have drawbacks that they cannot provide specific locations with local changes or defects. Therefore, we use Wavelet transform and calculate SAWP, then develop KPIs derived from SAWP for transition zone condition assessment for this study. The use of the 1/3 octave band is complementary and provides a good overview of the energy signals that can be used to analyze responses at the whole network-level.

7. Conclusion and future work

This paper proposes the design of KPIs for monitoring transition zones using multi-ABA measurements. The case study considers transition zones at railway bridges; however, the proposed KPI methodology can apply not only to the Dutch railway network where the soils are very soft, but also to monitor other railway lines and other types of transition zones between soil and rigid structures. Based on the analyses, the following conclusions can be drawn:

(1) A multi-ABA measurement system is promising for transition zone condition monitoring. Different transition zones show differences in ABA responses. From the analysis of such responses, the health condition of transition zones can potentially be evaluated using in-service trains with frequent and continuous measurements.

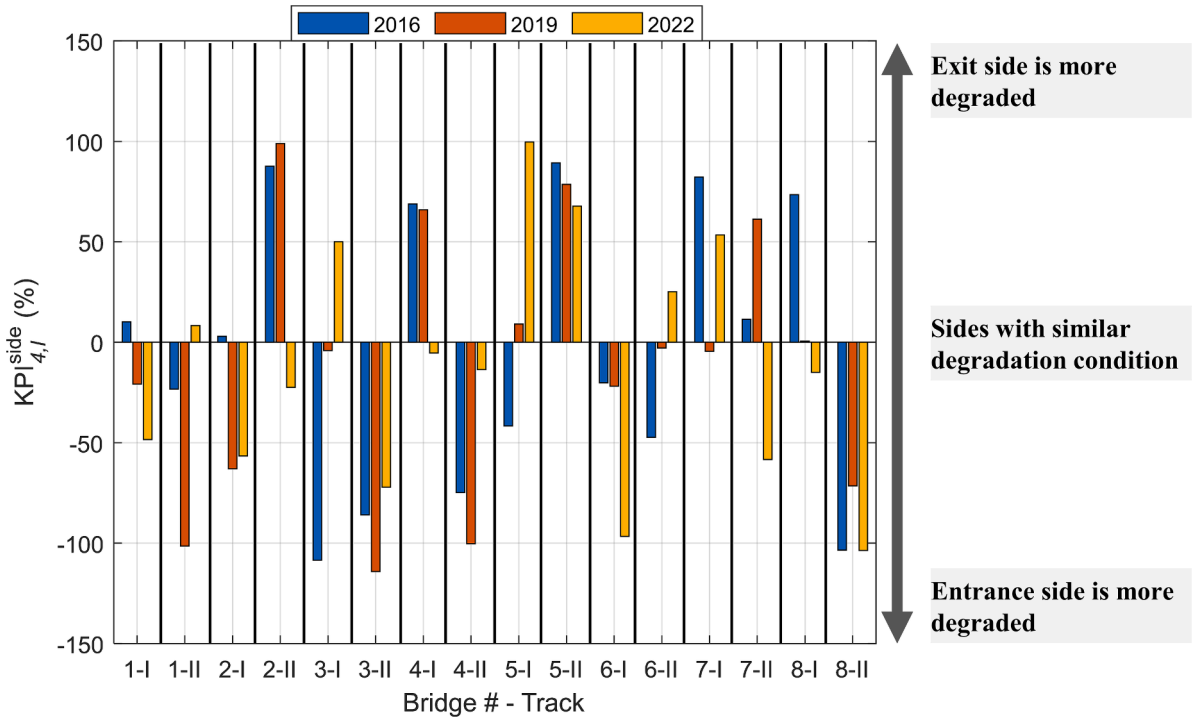

Fig. 22. KPI to evaluate substructure condition differences between sides from different measurement years.

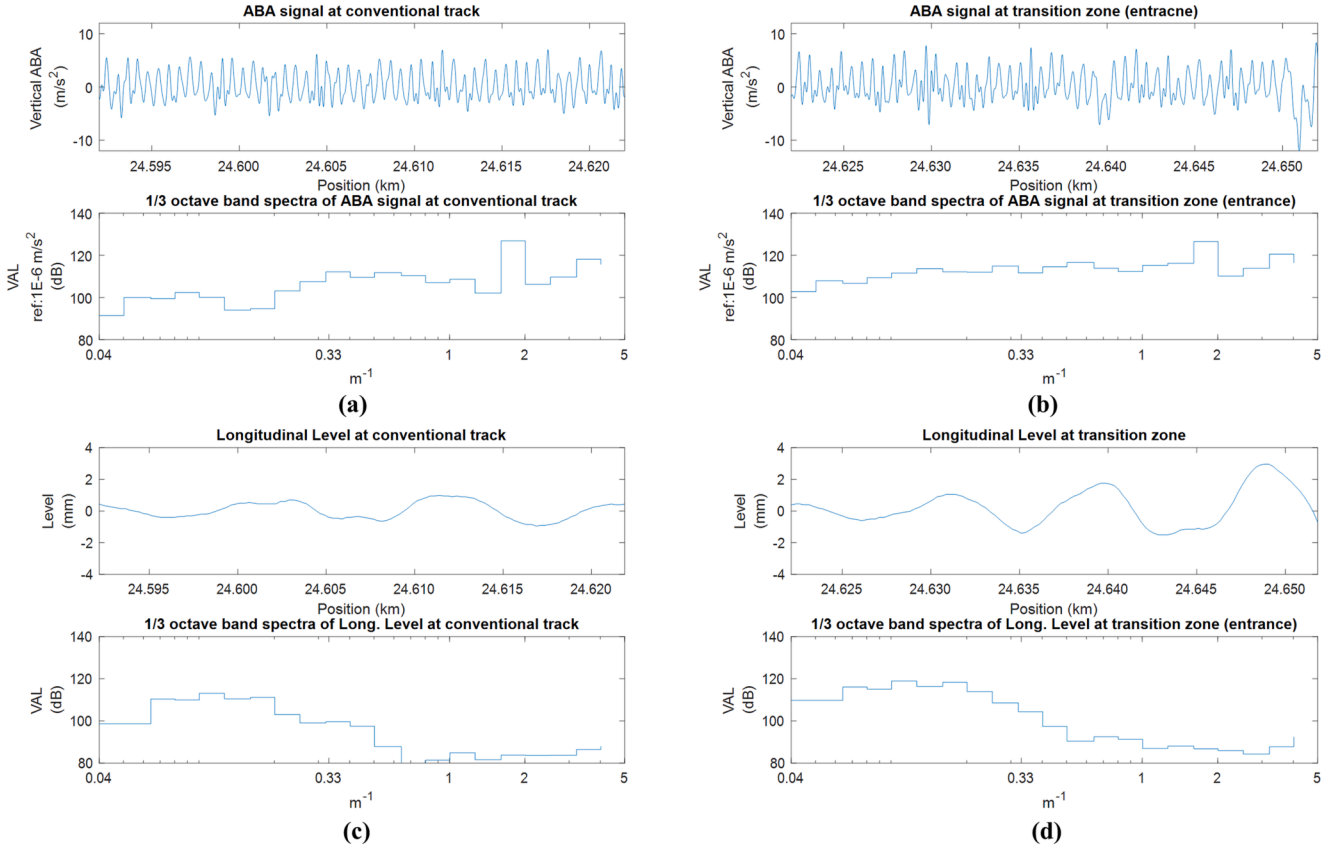

Fig. 23. Comparison of ABA and the longitudinal level response at the location nearby Bridge 6 in the time domain and the VAL (1/3 octave band): (a) ABA signal at the conventional track; (b) ABA signal at the entrance transition zone; (c) the longitudinal level at the conventional track; (d) the longitudinal level at the entrance transition zone.

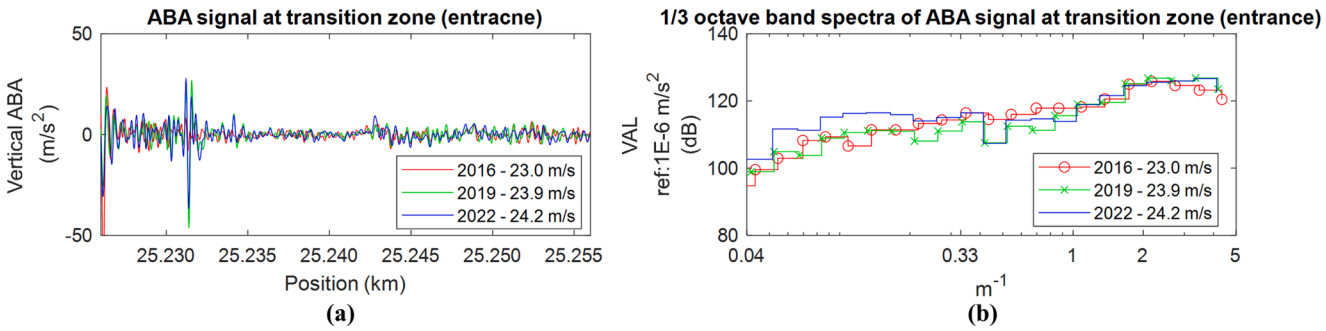

Fig. 24. Evolution of the entrance transition zone from 2016, 2019, and 2022: (a) ABA signals in the time domain; (b) the *VAL* of ABA signals.

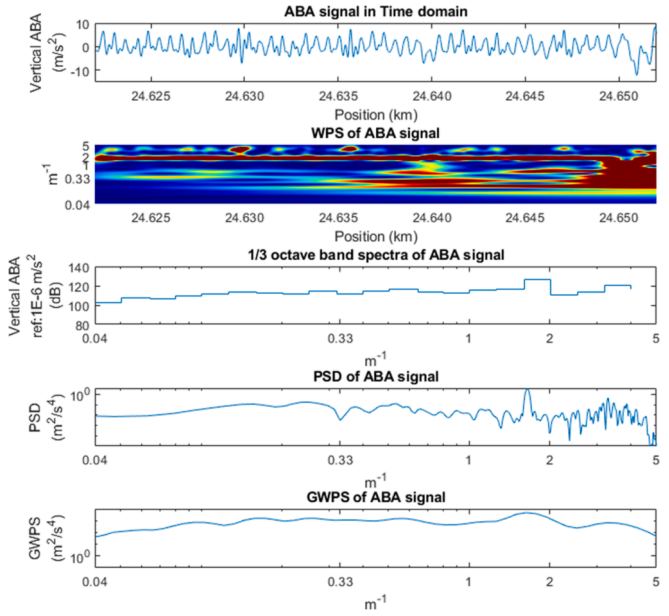

Fig. 25. ABA signal response in the frequency domain according to 3 different quantities at the entrance transition zone, Bridge 6.

(2) The measurement speed influences multi-ABA responses. A measurement at higher speed yields more prominent ABA responses at a particular location due to the higher excitation level in the low-frequency range, which helps distinguish the responses related to substructure conditions. Additionally, ABA responses vary when collected from different trains or with the same trains under different operational conditions. This factor must be considered when deriving KPIs from operational trains with different characteristics.

(3) For the considered spatial frequency range from 0.04 m^{-1} to 0.33 m^{-1}, the particular transition zones at each bridge exhibit different characteristics. These distributed characteristics pertain to each part of the transition zones and their health condition status.

(4) ABA energy-based KPIs allow the assessment of different degradation levels of transition zones from the large-scale level to the small-scale level, i.e., between different abutments of a particular bridge, between different tracks of a particular abutment, between different sides of a particular track, and between rails of a particular side.

(5) According to the case study, the locations with the highest degradation do not always occur at a specific abutment (North or South), track (Track I or II), side (entrance or exit), or rail (inner or outer). Further investigations at those locations could provide a better understanding of the degradation mechanisms at transition zones.

(6) The KPIs from different measurement years correlate with the track geometry-based quality index. Still, we observed locations where track geometry did not show important variations while ABA indicated stronger responses. The higher resolution of ABA might explain this (one measurement every 1.5 mm with 140 km/h measurement speed) compared to the track geometry measurement method (25 cm).

A portion of the corresponding planned future research includes further understanding of the effect of the measurement speed on multi-ABA responses. Other topics for further research are the fusion of data from the ABA measurement campaign with other inspection techniques. For instance, track geometry parameters, ground penetrating radar (GPR), and in-situ measurements are required to understand the degradation mechanism and the cause of the malfunctions of transition zones better. Thus, KPIs based on a sufficient understanding of the causes of malfunctions can be included as part of the condition-based maintenance criteria.

CRediT authorship contribution statement

Siwarak Unsiwilai: Conceptualization, Methodology, Software, Formal analysis, Data curation, Writing – original draft, Visualization. **Li Wang:** Conceptualization, Writing – original draft, Writing – review & editing. **Alfredo Núñez:** Conceptualization, Funding acquisition, Supervision, Methodology, Writing – review & editing. **Zili Li:** Conceptualization, Funding acquisition, Supervision, Methodology, Writing – review & editing.

Declaration of Competing Interest

The authors declare that they have no known competing financial interests or personal relationships that could have appeared to influence the work reported in this paper.

Data availability

Data will be made available on request.

Acknowledgements

The authors would like to thank the reviewers for their comments and suggestions for improving the quality of this manuscript. This research was partly supported by ProRail and Europe's Rail Flagship Project IAM4RAIL - Holistic and Integrated Asset Management for Europe's RAIL System [grant agreement 101101966]. The first author would like to thank the Royal Thai Government for the Ph.D. scholarship.

References

[1] T. Dahlberg, Railway Track Settlements-A Literature Review, Report for the EU project SUPERTRACK, Linkoping University Sweden, 2003.

[2] R. Sañudo, L. Dell'Olio, J.A. Casado, I.A. Carrascal, S. Diego, Track transitions in railways: a review, Constr. Build. Mater. 112 (2016) 140–157, https://doi.org/10.1016/j.conbuildmat.2016.02.084.

[3] A. Paixão, E. Fortunato, R. Calçada, Design and construction of backfills for railway track transition zones, Proc. Inst. Mech. Eng. Part F J. Rail Rapid Transit. 229 (2015) 58–70, https://doi.org/10.1177/0954409713499016.

[4] A. Paixão, E. Fortunato, R. Calçada, A numerical study on the influence of backfill settlements in the train/track interaction at transition zones to railway bridges, Proc. Inst. Mech. Eng. Part F J. Rail Rapid Transit. 230 (2016) 866–878, https://doi.org/10.1177/0954409715573289.

[5] J.Y. Zhu, D.J. Thompson, C.J.C. Jones, On the effect of unsupported sleepers on the dynamic behaviour of a railway track, Veh. Syst. Dyn. 49 (2011) 1389–1408, https://doi.org/10.1080/00423114.2010.524303.

[6] K.K. Ang, J. Dai, Response analysis of high-speed rail system accounting for abrupt change of foundation stiffness, J. Sound Vib. 332 (2013) 2954–2970, https://doi.org/10.1016/j.jsv.2013.01.005.

[7] Y. Bezin, S.D. Iwnicki, M. Cavalletti, E. de Vries, F. Shahzad, G. Evans, An investigation of sleeper voids using a flexible track model integrated with railway multi-body dynamics, Proc. Inst. Mech. Eng. Part F J. Rail Rapid Transit. 223 (2009) 597–607, https://doi.org/10.1243/09544097JRRT276.

[8] H. Wang, V. Markine, Dynamic behaviour of the track in transitions zones considering the differential settlement, J. Sound Vib. 459 (2019), 114863, https://doi.org/10.1016/j.jsv.2019.114863.

[9] P. Hölscher, P. Meijers, Literature study of knowledge and experience of transition zones, 2007.

[10] Y. Shan, Y. Shu, S. Zhou, Finite-infinite element coupled analysis on the influence of material parameters on the dynamic properties of transition zones, Constr. Build. Mater. 148 (2017) 548–558, https://doi.org/10.1016/j.conbuildmat.2017.05.071.

[11] A.B. Fărăgău, A.V. Metrikine, K.N. van Dalen, Transition radiation in a piecewise-linear and infinite one-dimensional structure–a Laplace transform method, Nonlinear Dyn. 98 (2019) 2435–2461, https://doi.org/10.1007/s11071-019-05083-6.

[12] H. Wang, V. Markine, Modelling of the long-term behaviour of transition zones: Prediction of track settlement, Eng. Struct. 156 (2018) 294–304, https://doi.org/10.1016/j.engstruct.2017.11.038.

[13] Y. Shan, S. Zhou, H. Zhou, B. Wang, Z. Zhao, Y. Shu, Z. Yu, Iterative method for predicting uneven settlement caused by high-speed train loads in transition-zone subgrade, Transp. Res. Rec. J Transp. Res. Board. 2607 (2017) 7–14, https://doi.org/10.3141/2607-02.

[14] A. Paixão, J.N. Varandas, E. Fortunato, R. Calçada, Numerical simulations to improve the use of under sleeper pads at transition zones to railway bridges, Eng. Struct. 164 (2018) 169–182, https://doi.org/10.1016/j.engstruct.2018.03.005.

[15] I. Gallego Giner, A. López Pita, Numerical simulation of embankment—structure transition design, Proc. Inst. Mech. Eng. Part F J. Rail Rapid Transit. 223 (2009) 331–343, https://doi.org/10.1243/09544097JRRT234.

[16] J.N. Varandas, P. Hölscher, M.A.G. Silva, Dynamic behaviour of railway tracks on transitions zones, Comput. Struct. 89 (2011) 1468–1479, https://doi.org/10.1016/j.compstruc.2011.02.013.

[17] Y. Shan, B. Albers, S.A. Savidis, Influence of different transition zones on the dynamic response of track–subgrade systems, Comput. Geotech. 48 (2013) 21–28, https://doi.org/10.1016/j.compgeo.2012.09.006.

[18] B. Coelho, P. Hölscher, J. Priest, W. Powrie, F. Barends, An assessment of transition zone performance, Proc. Inst. Mech. Eng. Part F J. Rail Rapid Transit. 225 (2011) 129–139, https://doi.org/10.1177/09544097JRRT389.

[19] T.D. Stark, S.T. Wilk, Root cause of differential movement at bridge transition zones, Proc. Inst. Mech. Eng. Part F J. Rail Rapid Transit. 230 (2016) 1257–1269, https://doi.org/10.1177/0954409715589620.

[20] C. Alves Ribeiro, R. Calçada, R. Delgado, Experimental assessment of the dynamic behaviour of the train-track system at a culvert transition zone, Eng. Struct. 138 (2017) 215–228, https://doi.org/10.1016/j.engstruct.2017.02.020.

[21] Y. Çati, S. Gökçeli, Ö. Anil, C.S. Korkmaz, Experimental and numerical investigation of USP for optimization of transition zone of railway, Eng. Struct. 209 (2020), 109971, https://doi.org/10.1016/j.engstruct.2019.109971.

[22] J. Mottahed, J.A. Zakeri, S. Mohammadzadeh, A field investigation on the effects of using USPs in transition zone from ballasted track to bridges, Int. J. Civ. Eng. 17 (2019) 1421–1431, https://doi.org/10.1007/s40999-019-00440-3.

[23] J. Shi, M.P.N. Burrow, A.H. Chan, Y.J. Wang, Measurements and simulation of the dynamic responses of a bridge–embankment transition zone below a heavy haul railway line, Proc. Inst. Mech. Eng. Part F J. Rail Rapid Transit. 227 (2013) 254–268, https://doi.org/10.1177/0954409712460979.

[24] H. Heydari-Noghabi, J. Zakeri, M. Esmaeili, J. Varandas, Field study using additional rails and an approach slab as a transition zone from slab track to the ballasted track, Proc. Inst. Mech. Eng. Part F J. Rail Rapid Transit. 232 (2018) 970–978, https://doi.org/10.1177/0954409717708527.

[25] C. Gallage, B. Dareeju, M. Dhanasekar, Track degradation a bridge transitions, in: K.P.P. Pathirana (Ed.), 4th Int. Conf. Struct. Eng. Constr. Manag., Nethwin Printers (Pvt) Ltd, Sri Lanka, 2013, pp. 40–52, https://eprints.qut.edu.au/70153/.

[26] P. Wang, L. Wang, R. Chen, J. Xu, J. Xu, M. Gao, Overview and outlook on railway track stiffness measurement, J. Mod. Transp. 24 (2016) 89–102, https://doi.org/10.1007/s40534-016-0104-8.

[27] S. Shao, D. Ji, Coupled discrete-finite element method for settlement analysis of transition zone between ballasted and ballastless track with polyurethane reinforcement based on computer aided technology, J. Phys. Conf. Ser. 1574 (2020), 012007, https://doi.org/10.1088/1742-6596/1574/1/012007.

[28] L. Auersch, Different types of continuous track irregularities as sources of train-induced ground vibration and the importance of the random variation of the track support, Appl. Sci. 12 (2022) 1463, https://doi.org/10.3390/app12031463.

[29] S. Park, J.Y. Kim, J. Kim, S. Lee, K.-H. Cho, Analysis of dynamic characteristics of deformed concrete slab track on transition zone in high-speed train line according to train speeds, Appl. Sci. 10 (2020) 7174, https://doi.org/10.3390/app10207174.

[30] H. Boler, D. Mishra, E. Tutumluer, S. Chrismer, J.P. Hyslip, Stone blowing as a remedial measure to mitigate differential movement problems at railroad bridge approaches, Proc. Inst. Mech. Eng. Part F J. Rail Rapid Transit. 233 (2019) 63–72, https://doi.org/10.1177/0954409718778654.

[31] A. Paixão, C. Alves Ribeiro, N. Pinto, E. Fortunato, R. Calçada, On the use of under sleeper pads in transition zones at railway underpasses: experimental field testing, Struct. Infrastruct. Eng. 11 (2015) 112–128, https://doi.org/10.1080/15732479.2013.850730.

[32] C. Zhao, P. Wang, Q. Yi, D. Meng, Application of polyurethane polymer and assistant rails to settling the abnormal vehicle-track dynamic effects in transition zone between ballastless and ballasted track, Shock Vib. 2015 (2015) 1–9, https://doi.org/10.1155/2015/826362.

[33] H. Heydari-Noghabi, J.N. Varandas, M. Esmaeili, J. Zakeri, Investigating the influence of auxiliary rails on dynamic behavior of railway transition zone by a 3D train-track interaction model, Lat. Am. J. Solids Struct. 14 (2017) 2000–2018, https://doi.org/10.1590/1679-78253906.

[34] H. Wang, V. Markine, Corrective countermeasure for track transition zones in railways: adjustable fastener, Eng. Struct. 169 (2018) 1–14, https://doi.org/10.1016/j.engstruct.2018.05.004.

[35] B. Indraratna, M. Babar Sajjad, T. Ngo, A. Gomes Correia, R. Kelly, Improved performance of ballasted tracks at transition zones: a review of experimental and modelling approaches, Transp. Geotech. 21 (2019), 100260, https://doi.org/10.1016/j.trgeo.2019.100260.

[36] C. Ngamkhanong, K. Goto, S. Kaewunruen, Dynamic responses of railway ballasted track considering rail pad deterioration, J. Phys. Conf. Ser. 1106 (2018), 012006, https://doi.org/10.1088/1742-6596/1106/1/012006.

[37] L. Auersch, Vehicle-track-soil interaction and train-induced ground vibration – theory and measurements in Germany, Switzerland and France, J. Phys. Conf. Ser. 1264 (2019), 012034, https://doi.org/10.1088/1742-6596/1264/1/012034.

[38] C. Shen, R. Dollevoet, Z. Li, Fast and robust identification of railway track stiffness from simple field measurement, Mech. Syst. Signal Process. 152 (2021), 107431, https://doi.org/10.1016/j.ymssp.2020.107431.

[39] S. Kaewunruen, A.M. Remennikov, Field trials for dynamic characteristics of railway track and its components using impact excitation technique, NDT E Int. 40 (2007) 510–519, https://doi.org/10.1016/j.ndteint.2007.03.004.

[40] R. Sañudo, I. Jardí, J.-C. Martínez, F.-J. Sánchez, M. Miranda, B. Alonso, L. Dell'Olio, J.-L. Moura, Monitoring track transition zones in railways, Sensors. 22 (2021) 76, https://doi.org/10.3390/s22010076.

[41] J.G. Rose, T.D. Stark, S.T. Wilk, M. Purcell, Design and monitoring of well-performing bridge transitions, in: 2015 Jt. Rail Conf., American Society of Mechanical Engineers, 2015: p. V001T01A007. https://doi.org/10.1115/JRC2015-5645.

[42] E. Tutumluer, T.D. Stark, D. Mishra, J.P. Hyslip, Investigation and mitigation of differential movement at railway transitions for US high speed passenger rail and joint passenger/freight corridors, in: 2012 Jt. Rail Conf., American Society of Mechanical Engineers, 2012, pp. 75–84. https://doi.org/10.1115/JRC2012-74074.

[43] D. Mishra, E. Tutumluer, H. Boler, J.P. Hyslip, T.R. Sussmann, Railroad track transitions with multidepth deflectometers and strain gauges, Transp. Res. Rec. J Transp. Res. Board. 2448 (2014) 105–114, https://doi.org/10.3141/2448-13.

[44] H. Wang, M. Silvast, V. Markine, B. Wiljanen, Analysis of the dynamic wheel loads in railway transition zones considering the moisture condition of the ballast and subballast, Appl. Sci. 7 (2017) 1208, https://doi.org/10.3390/app7121208.

[45] H. Wang, V. Markine, X. Liu, Experimental analysis of railway track settlement in transition zones, Proc. Inst. Mech. Eng. Part F J. Rail Rapid Transit. 232 (2018) 1774–1789, https://doi.org/10.1177/0954409717748789.

[46] H. Wang, L. Chang, V. Markine, Structural health monitoring of railway transition zones using satellite radar data, Sensors. 18 (2018) 413, https://doi.org/10.3390/s18020413.

[47] A. Rodríguez, R. Sañudo, M. Miranda, A. Gómez, J. Benavente, Smartphones and tablets applications in railways, ride comfort and track quality. Transition zones analysis, Measurement. 182 (2021), 109644, https://doi.org/10.1016/j.measurement.2021.109644.

[48] H. Wang, J. Berkers, N. van den Hurk, N.F. Layegh, Study of loaded versus unloaded measurements in railway track inspection, Measurement. 169 (2021), 108556, https://doi.org/10.1016/j.measurement.2020.108556.

[49] V.J. Hodge, S. O'Keefe, M. Weeks, A. Moulds, Wireless sensor networks for condition monitoring in the railway industry: a survey, IEEE Trans. Intell. Transp. Syst. 16 (2015) 1088–1106, https://doi.org/10.1109/TITS.2014.2366512.

[50] D. Seneviratne, L. Ciani, M. Catelani, D. Galar, Smart maintenance and inspection of linear assets: an Industry 4.0 approach, ACTA IMEKO. 7 (2018) 50, https://doi.org/10.21014/acta_imeko.v7i1.519.

[51] M. Kans, D. Galar, A. Thaduri, Maintenance 4.0 in railway transportation industry, in: K.T. Koskinen, H. Kortelainen, J. Aaltonen, T. Uusitalo, K. Komonen, J. Mathew, J. Laitinen (Eds.), Lect. Notes Mech. Eng, Springer International Publishing, Cham, 2016, pp. 317–331, https://doi.org/10.1007/978-3-319-27064-7_30.

[52] M. Molodova, Z. Li, R. Dollevoet, Axle box acceleration: measurement and simulation for detection of short track defects, Wear. 271 (2011) 349–356, https://doi.org/10.1016/j.wear.2010.10.003.

[53] M. Molodova, Z. Li, A. Nunez, R. Dollevoet, Automatic detection of squats in railway infrastructure, IEEE Trans. Intell. Transp. Syst. 15 (2014) 1980–1990, https://doi.org/10.1109/TITS.2014.2307955.
[54] P. Salvador, V. Naranjo, R. Insa, P. Teixeira, Axlebox accelerations: their acquisition and time–frequency characterisation for railway track monitoring purposes, Measurement. 82 (2016) 301–312, https://doi.org/10.1016/j.measurement.2016.01.012.
[55] A. Nunez, A. Jamshidi, H. Wang, Pareto-based maintenance decisions for regional railways with uncertain weld conditions using the hilbert spectrum of axle box acceleration, IEEE Trans. Ind. Informatics. 15 (2019) 1496–1507, https://doi.org/10.1109/TII.2018.2847736.
[56] Z. Li, M. Molodova, A. Nunez, R. Dollevoet, Improvements in axle box acceleration Measurements for the Detection of Light Squats in Railway Infrastructure, IEEE Trans. Ind. Electron. 62 (2015) 4385–4397, https://doi.org/10.1109/TIE.2015.2389761.
[57] M. Molodova, M. Oregui, A. Núñez, Z. Li, R. Dollevoet, Health condition monitoring of insulated joints based on axle box acceleration measurements, Eng. Struct. 123 (2016) 225–235, https://doi.org/10.1016/j.engstruct.2016.05.018.
[58] Z. Wei, A. Núñez, Z. Li, R. Dollevoet, Evaluating degradation at railway crossings using axle box acceleration measurements, Sensors. 17 (2017) 2236, https://doi.org/10.3390/s17102236.
[59] M. Oregui, S. Li, A. Núñez, Z. Li, R. Carroll, R. Dollevoet, Monitoring bolt tightness of rail joints using axle box acceleration measurements, Struct. Control Heal. Monit. 24 (2017) e1848, https://doi.org/10.1002/stc.1848.
[60] D. Li, J. Hyslip, T. Sussmann, S. Chrismer, Railway geotechnics, CRC Press, 2015.
[61] CEN, NEN-EN 13848-1:2019 en - Railway applications - Track - Track geometry quality - Part 1: Characterization of track geometry, (2019). https://www.nen.nl/en/nen-en-13848-1-2019-en-257518.
[62] J.C.O. Nielsen, E.G. Berggren, A. Hammar, F. Jansson, R. Bolmsvik, Degradation of railway track geometry – correlation between track stiffness gradient and differential settlement, Proc. Inst. Mech. Eng. Part F J. Rail Rapid Transit. 234 (2020) 108–119, https://doi.org/10.1177/0954409718819581.
[63] K. Chen, B. Lechner, DESTination RAIL – Decision Support Tool for Rail Infrastructure Managers: D2.4 Report on Assessment of Track, 2017. https://ec.europa.eu/research/participants/documents/downloadPublic?documentIds=080166e5b760cf70&appId=PPGMS.
[64] C. Esveld, Modern Railway Track, second ed., MRT-productions, Zaltbommel, 2003.
[65] C. Charoenwong, D.P. Connolly, P.K. Woodward, P. Galvín, P. Alves Costa, Analytical forecasting of long-term railway track settlement, Comput. Geotech. 143 (2022), 104601, https://doi.org/10.1016/j.compgeo.2021.104601.
[66] Z. Li, M. Molodova, Method and instrumentation for detection of rail defects, in particular rail top defects, WO 2011019273 (A1) (2011). http://resolver.tudelft.nl/uuid:5b2dcfc2-a584-4690-acad-4d6aa1056dc7.
[67] E. Arlaud, S. Costa D'Aguiar, E. Balmes, Receptance of railway tracks at low frequency: Numerical and experimental approaches, Transp. Geotech. 9 (2016) 1–16, https://doi.org/10.1016/j.trgeo.2016.06.003.
[68] L. Wang, P. Wang, K. Wei, R. Dollevoet, Z. Li, Ground vibration induced by high speed trains on an embankment with pile-board foundation: Modelling and validation with in situ tests, Transp. Geotech. 34 (2022), 100734, https://doi.org/10.1016/j.trgeo.2022.100734.
[69] E.G. Berggren, A.M. Kaynia, B. Dehlbom, Identification of substructure properties of railway tracks by dynamic stiffness measurements and simulations, J. Sound Vib. 329 (2010) 3999–4016, https://doi.org/10.1016/j.jsv.2010.04.015.
[70] C. Torrence, G.P. Compo, A Practical Guide to Wavelet Analysis, Bull. Am. Meteorol. Soc. 79 (1998) 61–78, https://doi.org/10.1175/1520-0477(1998)079<0061:APGTWA>2.0.CO;2.
[71] D. Li, D. Davis, Transition of Railroad Bridge Approaches, J. Geotech. Geoenvironmental Eng. 131 (2005) 1392–1398, https://doi.org/10.1061/(ASCE)1090-0241(2005)131:11(1392).
[72] M. Audley, J.D. Andrews, The effects of tamping on railway track geometry degradation, Proc. Inst. Mech. Eng. Part F J. Rail Rapid Transit. 227 (2013) 376–391, https://doi.org/10.1177/0954409713480439.
[73] A. Paixão, E. Fortunato, R. Calçada, A contribution for integrated analysis of railway track performance at transition zones and other discontinuities, Constr. Build. Mater. 111 (2016) 699–709, https://doi.org/10.1016/j.conbuildmat.2016.02.126.
[74] L. Auersch, Excitation of ground vibration due to the passage of trains over a track with trackbed irregularities and a varying support stiffness, Veh. Syst. Dyn. 53 (2015) 1–29, https://doi.org/10.1080/00423114.2014.968173.
[75] L. Lazarević, D. Vučković, M. Vilotijević, Z. Popović, Application of seismic tomography for assessment of the railway substructure condition, Struct. Heal. Monit. 18 (2019) 792–805, https://doi.org/10.1177/1475921718774778.
[76] J. Náprstek, L. Frýba, Stochastic Modelling of Track and its Substructure, Veh. Syst. Dyn. 24 (1995) 297–310, https://doi.org/10.1080/00423119508969632.
[77] M. Ma, M. Li, X. Qu, H. Zhang, Effect of passing metro trains on uncertainty of vibration source intensity: monitoring tests, Measurement. 193 (2022), 110992, https://doi.org/10.1016/j.measurement.2022.110992.